MICROCOPY RESOLUTION TEST CHART
NATIONAL BUREAU OF STANDARDS-1963-A

Report R83-920021-F

COMPUTATION OF THE TIP VORTEX GENERATION PROCESS
FOR SHIP PROPELLER BLADES

T. R. Govindan, R. Levy and S. J. Shamroth
Scientific Research Associates, Inc.
Glastonbury, CT   06033

April 1984

AD-A141 069

DTIC
ELECTE
S MAY 1 4 1984 **D**
B

Prepared for:

The Office of Naval Research
Department of the Navy

DTIC FILE COPY

REPOh. DOCUMENTATION PAGE

READ INSTRUCTIONS
BEFORE COMPLETING FORM

1. REPORT NUMBER	2. GOVT ACCESSION NO.	3. RECIPIENT'S CATALOG NUMBER
R83-920021-F	*A141069*	

4. TITLE (and Subtitle)	5. TYPE OF REPORT & PERIOD COVERED
Computation of the Tip Vortex Generation Process for Ship Propeller Blades	Final Report (SBIR Phase I)
	6. PERFORMING ORG. REPORT NUMBER R83-920021-F

7. AUTHOR(s)	8. CONTRACT OR GRANT NUMBER(s)
T. R. Govindan, R. Levy and S. J. Shamroth	N00014-83-C-0768

9. PERFORMING ORGANIZATION NAME AND ADDRESS	10. PROGRAM ELEMENT, PROJECT, TASK AREA & WORK UNIT NUMBERS
Scientific Research Associates, Inc. P.O. Box 498 - 100 Sycamore Street Glastonbury, CT 06033	

11. CONTROLLING OFFICE NAME AND ADDRESS	12. REPORT DATE
Office of Naval Research 800 North Quincy Street Arlington, VA 22217	April 1984
	13. NUMBER OF PAGES 49

14. MONITORING AGENCY NAME & ADDRESS(if different from Controlling Office)	15. SECURITY CLASS. (of this report)
	Unclassified
	15a. DECLASSIFICATION/DOWNGRADING SCHEDULE

16. DISTRIBUTION STATEMENT (of this Report)

Approved for Public Release: Distribution Unlimited.

17. DISTRIBUTION STATEMENT (of the abstract entered in Block 20, if different from Report)

18. SUPPLEMENTARY NOTES

19. KEY WORDS (Continue on reverse side if necessary and identify by block number)

Tip vortex generation
Ship propeller
Forward marching procedure
Tip vortex
Propeller

20. ABSTRACT (Continue on reverse side if necessary and identify by block number)

⟶ A forward marching computation procedure has been used to compute the tip vortex generation process for ship propeller blades. Governing equations are derived through approximations to the Navier-Stokes equations made relative to a curvilinear coordinate system fitted to and aligned with the flow geometry. The approximations permit a forward marching solution of the governing equations thereby providing an economical and accurate method to compute many three-dimensional viscous flows.

(Continued)

DD FORM 1473 EDITION OF 1 NOV 65 IS OBSOLETE
1 JAN 73

Under the Phase I effort of the study, the forward marching procedure was extended to rotating coordinate systems. A geometry package was developed to describe the propeller tip and generate a suitable computation grid. Three test cases were run demonstrating the capability of the forward marching procedure to compute the tip vortex generation process. The capability of the method to compute the low pressure region at the center of the tip vortex was also demonstrated. The low pressure region is susceptible to cavitation.

DTIC
S ELECTE D
MAY 1 4 1984
B

Accession For
NTIS CRA&I	☑
DTIC TAB	☐
Unannounced	☐
Justification	

By_____
Distribution/
Availability Codes

| Dist | Avail and/or Special |
| A-1 | |

TABLE OF CONTENTS

1. INTRODUCTION

The tip vortex flow field plays a significant role in the performance of a ship propeller. The low pressure region found at the center of a tip vortex may lead to cavitation. The presence of cavitation in the flow field has serious consequences in terms of structural, acoustic, and performance considerations. A better understanding of the tip vortex generation process and a method of analysing the tip vortex flow field would provide valuable help in the design of the ship propeller.

The generation of a tip vortex can be found in a variety of hydrodynamic and aerodynamic airfoil type configurations. Typical examples can be found associated with the ship or submarine propeller, the submarine sail, the wing tip of fixed wing aircraft, and the helicopter rotor blade. These flow fields are characterized by a pressure differential across all inboard sections of the blade. Since at the blade tip a pressure discontinuity is not possible, the pressure difference across the blade is gradually relieved towards the tip until the pressures on both sides are equal at the tip. Associated with this pressure field is a secondary flow field outward on the pressure surface, around the tip, and inward on the suction surface. The secondary flow convects low momentum fluid from the pressure side around the tip to the suction side. The low momentum fluid accumulates on the suction side of the tip, rolls up and forms the tip vortex. The tip vortex is convected downstream by the streamwise velocity.

The flow field in the tip region is complex, three-dimensional, and viscous with large secondary velocities. The large secondary velocities preclude the possibility of using conventional boundary layer solution techniques to compute the tip vortex flow. On the other hand, a solution of the full Navier-Stokes equations that adequately resolves the tip vortex flow field would require formidable computational resources. Therefore, an approximate set of three-dimensional viscous flow equations which is applicable to the tip vortex flow field but which does not require the resources needed for the solution of the full Navier-Stokes equations is sought. The parabolized Navier-Stokes equations represent such a set. These equations contain in them all the physical processes of tip vortex generation and can be solved economically by forward marching procedures. This report examines the attractive possibility of using a forward marching procedure to compute the tip vortex generation process.

1

1.1 Objectives

The overall objective of the present effort is to compute the tip vortex generation process for ship propeller blades. This overall objective requires several stages of effort. The specific objectives undertaken in the present Phase I effort represented the first stage in the overall effort. These objectives were:

(a) Extension of an existing analysis to rotating coordinate systems. A rotating coordinate system fixed to the rotating propeller blade is a convenient coordinate system in which to describe the propeller tip flow field. Appropriate governing equations for the flow were formulated in the rotating coordinate system.

(b) Development of a geometry package to describe the propeller blade geometry in the computer code. A computational grid capable of resolving the tip vortex flow must be generated by the geometry package. This requires a grid generation procedure flexible enough to cluster grid points in regions of expected high gradients in the flow field.

(c) With the achievement of the above two objectives, the final objective under Phase I of the program was computation of the tip vortex generation process for a rotating ship propeller blade.

The scope of the proposed objectives was to demonstrate the capability of computing the tip vortex generation process for ship propeller blades by a forward marching procedure. The accomplishment of these objectives are documented in this report.

An additional portion of the Phase I effort was the computation of the pressure field and the surface pressure distribution on the blade produced by the tip vortex flow. This computation provides the capability of identifying low pressure regions in the flow that may be susceptible to cavitation. Results from this effort are also documented in this report.

1.2 Outline of the Phase I Program

A step-by-step approach was adopted to accomplish the specific objectives of the Phase I program detailed in the previous section. Specific

2

tasks were identified to define the steps of the approach. These tasks were the following:

(a) Addition of the rotation terms in the governing equations,

(b) Verification of the rotation terms by computing a known flow field,

(c) Computation of the flow over a circular cross section tip,

(d) Development of a geometry package for the propeller tip flow field computation,

(e) Computation of the tip vortex flow field for a straight blade with a rounded tip,

(f) Computation of the tip vortex flow field for a rotating straight blade with a rounded tip, and

(g) Computation of the tip vortex flow field for a rotating twisted blade with a rounded tip.

Tasks (a) and (b) accomplished the extension of the existing forward marching procedure to rotating coordinate systems. Task (c) verified the ability of the forward marching procedure to compute the flow processes in vortex generation without the additional complexities of the propeller geometry. Task (d) developed a geometry package capable of describing the propeller tip geometry in the computer code and the generation of a suitable computation grid for the tip vortex flow field. Tasks (e), (f) and (g) computed the tip vortex flow field in stages of increasing complexity. A detailed description of the tasks and the results of the tasks are documented in this report.

2. THE FORWARD MARCHING COMPUTATION PROCEDURE FOR SHIP PROPELLER TIP FLOW FIELDS

The forward marching computation procedure for the solution of the parabolized Navier-Stokes equation provides an economical and accurate method for computing many three-dimensional viscous flow fields. The procedure, initially developed for internal flow fields, was extended to the computation of the ship propeller tip flow field under the Phase I work plan. The governing equations, the computation scheme, and results from the procedure are presented in this section. The procedure is capable of considering both fixed and rotating coordinate systems.

The governing equations are derived through approximations made relative to a curvilinear coordinate system fitted to and aligned with the flow geometry under consideration. The coordinate system is chosen such that the streamwise or marching coordinate either coincides with or is at least approximately aligned with a known inviscid primary flow direction as determined, for example, by a potential flow for the given geometry. Transverse coordinate surfaces must be approximately perpendicular to solid walls or bounding surfaces, since diffusion is permitted only in these transverse coordinate surfaces.

Equations governing primary flow velocity U_p, and a secondary vorticity, Ω_n, normal to transverse coordinate surfaces are derived utilizing approximations which permit solution of the correction equations as an initial-value problem, provided reversal of the composite streamwise velocity does not occur. Terms representing diffusion normal to transverse coordinate surfaces (in the streamwise direction) are neglected. Secondary flow velocities are determined from scalar and vector surface potential calculations in transverse coordinate surfaces, once the primary velocity and secondary vorticity are known.

Primary-Secondary Velocity Decomposition

In what follows, vectors are denoted by an overbar, and unit vectors by a caret. The analysis is based on decomposition of the overall velocity vector field $\bar{U}$ into a primary flow velocity $\bar{U}_p$ and a secondary flow

4

velocity $\bar{U}_s$. The overall or composite velocity is determined from the superposition

$$\bar{U} = \bar{U}_p + \bar{U}_s \tag{1}$$

The primary flow velocity is represented as

$$\bar{U}_p = U_p \hat{i}_p \tag{2}$$

where $\hat{i}_p$ is a known inviscid primary flow direction determined for example from an _a priori_ potential flow solution for the geometry under consideration. A streamwise coordinate direction from a body fitted coordinate system could be used as an approximation to this potential flow direction. The primary velocity U_p is determined from solution of a primary flow momentum equation. The secondary flow velocity $\bar{U}_s$ is derived from scalar and vector surface potential denoted ϕ and ψ, respectively. If $\hat{i}_n$ denotes the unit vector normal to transverse coordinate surfaces, if ρ is density, and if ρ_o is an arbitrary constant reference density, then $\bar{U}_s$ is defined by

$$\bar{U}_s \equiv \nabla_s \phi + (\rho_o/\rho)\nabla \times \hat{i}_n \psi \tag{3}$$

where ∇_s is the surface gradient operator defined by

$$\nabla_s \equiv \nabla - \hat{i}_n (\hat{i}_n \cdot \nabla) \tag{4}$$

It follows that since $\hat{i}_n \cdot \bar{U}_s = 0$, then U_s lies entirely within transverse coordinate surfaces. Equation (3) is a general form permitting bo' rotational and irrotational secondary flows and will lead to governing equations which may be solved as an initial-boundary value problem. The overall velocity decomposition (1) can be written

$$\bar{U} = U_p \hat{i}_p + \nabla_s \phi + (\rho_o/\rho)\nabla \times \hat{i}_n \psi \tag{5}$$

5

Surface Potential Equations

Equations relating ϕ and ψ with U_p, ρ, and the secondary vorticity component Ω_n can be derived using Eq. (5) as follows: From continuity,

$$\nabla \cdot \rho \bar{U} = 0 = \nabla \cdot \rho U_p \hat{i}_p + \nabla \cdot \rho \nabla_s \phi + \rho_o \nabla \cdot \nabla x \hat{i}_n \psi \qquad (6)$$

and from the definition of the vorticity based on the secondary flow within the transverse surfaces, Ω_n

$$\hat{i}_n \cdot \nabla x \bar{U} \equiv \Omega_n = \hat{i}_n \cdot \nabla x\; U_p \hat{i}_p + \hat{i}_n \cdot \nabla x (\rho_o/\rho)\; \nabla x\; \hat{i}_n \psi + \hat{i}_n \cdot \nabla \times \nabla_s \phi \qquad (7)$$

Since the last term in each of Eqs. (6 and 7) is zero by vector identity, Eqs. (6 and 7) can be written as

$$\nabla \cdot \rho \nabla_s \phi = -\nabla \cdot \rho U_p \hat{i}_p \qquad (8)$$

$$\hat{i}_n \cdot \nabla x\; (\rho_o/\rho)\; \nabla x \hat{i}_n \psi = \Omega_n - \hat{i}_n \cdot \nabla x\; U_p \hat{i}_p \qquad (9)$$

Note that the last term in Eq. (9) is identically zero in a coordinate system for which $\hat{i}_n$ and $\hat{i}_p$ have the same direction, and would be small if $\hat{i}_n$ and $\hat{i}_p$ are approximately aligned. In any event, given a knowledge of U_p, Ω_n and ρ, the surface potentials ϕ and ψ can be determined by a two-dimensional elliptic calculation in transverse coordinate surfaces at each streamwise location. In turn, $\bar{U}_s$ can be computed from Eq. (3), and the composite velocity $\bar{U}$ will satisfy continuity. Equations for U_p and Ω_n are obtained from the equations governing momentum and vorticity, respectively.

The streamwise momentum equation is given by

$$\hat{i}_p \cdot [\; (\bar{U} \cdot \nabla)\bar{U} + (\nabla P)/\rho] = \hat{i}_p \cdot \bar{F} + \hat{i}_p \cdot \bar{R} \qquad (10)$$

where P is pressure and ρF is force due to viscous stress and terms in F representing streamwise diffusion are neglected. $\rho \bar{R}$ is the additional force due to a rotating coordinate system; where $\bar{R} = -2\bar{\omega} \times \bar{U} - \bar{\omega} \times (\bar{\omega} \times \bar{r})$, ω is the angular velocity of the coordinate system and $\bar{r}$ is the radius vector from the rotation axis. The pressure term in the streamwise momentum equation (10) can be taken from a simpler analysis such as a potential flow analysis. While this results in a set of equations which can be solved by forward marching, the surface pressures which are due to the pressure field imposed upon the flow are the potential flow pressures. Since the actual surface pressures are often of primary interest, a new estimate of the actual surface pressure which includes viscous and secondary flow effects can be compute from the resulting velocity field in the following manner.

The momentum equations in the transverse surfaces are:

$$\hat{i}_1 \cdot [(\rho \bar{U} \cdot \nabla) \bar{U} + \nabla P - \rho \bar{F} - \rho \bar{R}] = 0 \tag{11}$$

$$\hat{i}_2 \cdot [(\rho \bar{U} \cdot \nabla) \bar{U} + \nabla P - \rho \bar{F} - \rho \bar{R}] = 0$$

Equation (11) represents components of the momentum vector in the transverse surfaces:

$$\hat{i}_1 \, (\hat{i}_1 \cdot [(\rho \bar{U} \cdot \nabla) \bar{U} + \nabla P - \rho \bar{F} - \rho \bar{R}]) + \hat{i}_2 \, (\hat{i}_2 \cdot [(\rho \bar{U} \cdot \nabla) \bar{U} + \nabla P - \rho \bar{F} - \rho \bar{R}]) \tag{12}$$

The divergence of this vector can be written as a Poisson equation for the pressure P at each transverse surface:

$$\nabla_s^2 P = \nabla_s^2 (P_I + P_c) = -\frac{\partial}{\partial x_1} \, (\hat{i}_1 \cdot [(\rho \bar{U} \cdot \nabla) \bar{U} - \rho \bar{F} - \rho \bar{R}])$$

$$- \frac{\partial}{\partial x_2} \, (\hat{i}_2 \cdot [(\rho \bar{U} \cdot \nabla) \bar{U} - \rho \bar{F} - \rho \bar{R}]) \tag{13}$$

where P_I is the imposed pressure, P_c is a viscous correction to the pressure field and x_1 and x_2 are coordinates in the $\hat{i}_1$ and $\hat{i}_2$ directions, respectively. Equation (13) can be solved for the pressure correction, P_c, at each computational station using Neuman boundary conditions derived from Eq. (12). The use of Neuman boundary conditions

requires an additional parameter which is only a function of the normal direction, $P_v(x_3)$, in order to set the level of the pressure field. For internal flows $P_v(x_3)$ can be set to ensure that an integral mass flux condition is satisfied

$$\int_A \hat{i}_n \cdot \rho \bar{U} \, dA = CONSTANT \tag{14}$$

For external flows $P_v(x_3)$ can be set to match the imposed pressure at an appropriate far field location.

Secondary Vorticity

The equation governing Ω_n is obtained by cross differentiating each of the transverse momentum equations (11). Eliminating the pressure in the two equations results in a single equation for the transport of the vorticity normal to the transverse surface. This equation has the form

$$\bar{U} \cdot \nabla \Omega_n - \bar{\Omega} \cdot \nabla U_n = G_n + C + \hat{i}_n \cdot (\nabla X \bar{R}) \tag{15}$$

where G_n is the normal component of

$$\bar{G} = \nabla \times \bar{F} \tag{16}$$

and C is a collection of curvature terms arising from changes in orientation of the transverse surfaces as a function of streamwise coordinate.

Governing System of Equations

A complete system of four coupled equations governing U_p, Ω_n, ϕ and ψ is given by Eqs. (8), (9), (10) and (16). Ancillary relations are given by Eq. (5) for composite velocity and Eq. (14) for mass flux. In reference 1, these equations are given in general orthogonal coordinates and in reference 2 in nonorthogonal coordinates.

Numerical Method

Since techniques for obtaining the basic potential flow solution are well known and numerous, they need not be enumerated or discussed here.

Instead, the present development concentrates on describing the numerical method used to solve the system of correction equations. Streamwise derivative terms in the governing equations have a form such as $u_1 \partial(\ )/\partial x_1$, and because the streamwise velocity u_1 is very small in the viscous dominated region near no-slip walls, it is essential to use implicit algorithms which are not subject to stringent stability restrictions unrelated to accuracy requirements. Although it is possible to devise algorithms for solution of the correction equations as a fully coupled implicit system, such algorithms would require considerable iteration for the system of equations treated here, and this would detract from the overall efficiency. The present method is semi-implicit and seeks to reduce the amount of iteration required and yet avoid the more severe stability restrictions of explicit algorithms. The method partitions the system of correction equations into subsystems which govern the primary flow, the secondary flow, and the turbulence model. The primary-flow subset of equations contains the streamwise momentum equation. The secondary-flow subset of equations contains the secondary vorticity equation and the scalar and vector potential equations. These subsystems are decoupled using an ad hoc linearization in which secondary velocity components and turbulent viscosity are lagged, and are solved sequentially during each axial step.

Summary of Algorithm

The correction equations are replaced by finite-difference approximations. Three-point central difference formulas are used for all transverse spatial derivatives. Analytical coordinate transformations are employed as a means of introducing a nonuniform grid in each transverse coordinate direction, as appropriate, to concentrate grid points in the wall boundary layer regions. Second-order accuracy for the transverse directions is rigorously maintained. Two-point backward difference approximations are used for streamwise derivatives, although this is not essential.

To solve the primary flow subsystem of viscous correction equations for external flows, scalar ADI schemes are used for the momentum equation.

Given the solution for the primary flow, the secondary flow subsystem can be solved. First, the scalar potential equation (continuity) is solved

9

using a scalar iterative ADI scheme. Next, the secondary vorticity and vector potential equations are written as a ɹ!ly implicit coupled system and solved using an iterative linearized block implicit (LBI) scheme (cf. Briley and McDonald (3)). In selecting boundary conditions for the secondary flow subsystem, care must be taken to ensure that the final secondary velocity satisfies the no-slip condition accurately. Zero normal derivatives of ϕ are specified in the scalar potential equation, and this boundary condition corresponds to zero normal velocity. It is not possible to simultaneously specify the tangential velocity, however, and thus the ϕ-contribution to the secondary velocity will have a nonzero tangential (slip) component, denoted v_t, at solid boundaries. In the coupled vorticity and vector-potential equations, both normal and tangential velocity components can be specified as boundary conditions, since these equations are solved as a coupled system. By choosing (a) zero normal velocity, and (b) $-v_t$ as the ψ-contribution to the tangential velocity, the slip velocity v_t arising from the ϕ calculation is cancelled, and the composite secondary flow velocity including both ϕ and ψ contributions will satisfy the no-slip condition exactly.

A summary of the overall algorithm used to advance the solution a single axial step follows. It is assumed that the solution is known at the n-level x^n and is desired at x^{n+1}.

(1) The imposed streamwise pressure gradient distribution is determined from an a priori inviscid potential flow.

(2) The momentum equation is solved to determine u^{n+1}.

(3) Using values now available for ρ^{n+1} and u^{n+1}, the scalar potential equation (8) is solved using an iterative scalar ADI scheme, to obtain ϕ^{n+1}. This ensures that the continuity equation is satisfied.

(4) The equations for vorticity (16) and vector potential (9) form a coupled system for Ω^{n+1} and ψ^{n+1} which is solved as a coupled system using an iterative LBI scheme.

(5) Values for the transverse velocities v_s and w_s are computed from Eq. (3).

3. PRELIMINARY COMPUTATIONS

The previous section described the forward marching procedure along with the extension of the procedure to rotating coordinate systems. As mentioned previously, a rotating coordinate system is required for the analysis of the propeller tip flow field. The forward marching procedure has been used to compute a number of internal flow fields and has shown good qualitative and quantitative agreement with experimental data [2]. However, the formulation and coding of the rotation terms had not been verified. Further, a simple feasibility computation had to be performed to verify the capability of the analysis to compute the vortex generation process without the added complexity of the tip geometry. The results of this effort are described in this section.

3.1 Verification of the Rotation Terms

Simple test cases were chosen to verify the coding of the rotation terms in the equations. These cases correspond to the cases presented by Speziale [Ref. 4] who computed the fully developed flow in rotating ducts by a two-dimensional time-marching technique. This test case provided a geometrically simple configuration to compute the effects of rotation in the PEPSIG code. Further, these test cases had been computed successfully by McDonald, Briley and Lin [Ref. 5] to verify the effect of rotation in an orthogonal version of this forward marching code. The computations were marched downstream until a fully-developed flow field was obtained for comparison with the computations of Speziale [Ref. 4].

Figure 2 shows a contour plot of the fully-developed streamwise velocity field in the duct for a Reynolds number of 235 and a Rossby number of 50.5. This Rossby number corresponds to a case of weak rotation effects on the flow field. An interesting point to be noted in Figure 2 is the shift of the contours away from the centerline of the duct, an effect purely from the rotation of the duct. In the case of a non-rotating duct the streamwise velocity contours would be symmetric about the centerline of the duct. Figure 3 compares a plot of the streamwise velocity along the centerline of the duct with the computations of Speziale. The two computations compare well with each other. The shift of the peak streamwise velocity away from
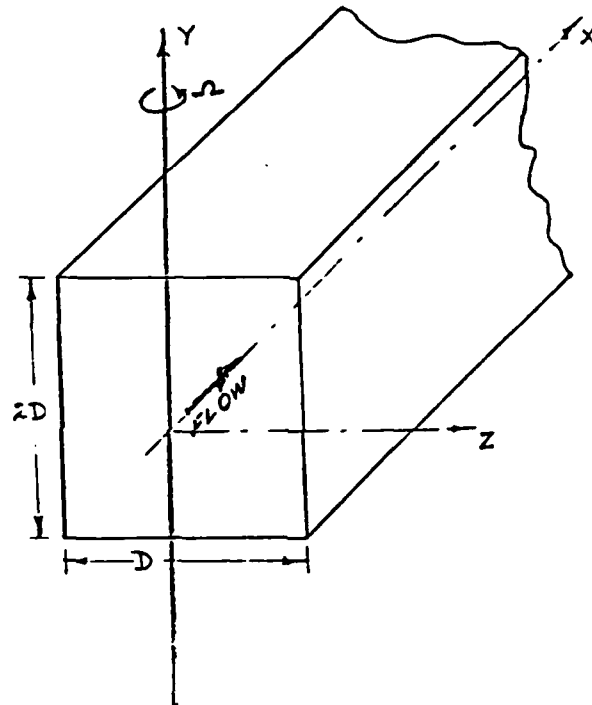
11

Figure 1 - Flow in a rotating duct - Configuration.
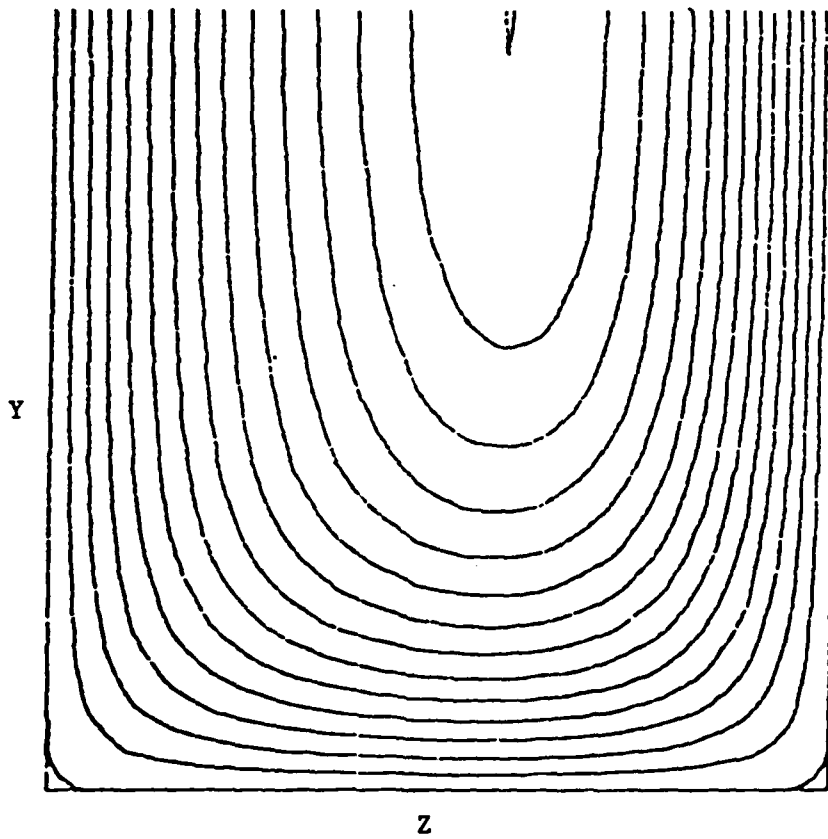
Maximum Velocity $= (U/\bar{U}) \approx 1.945$

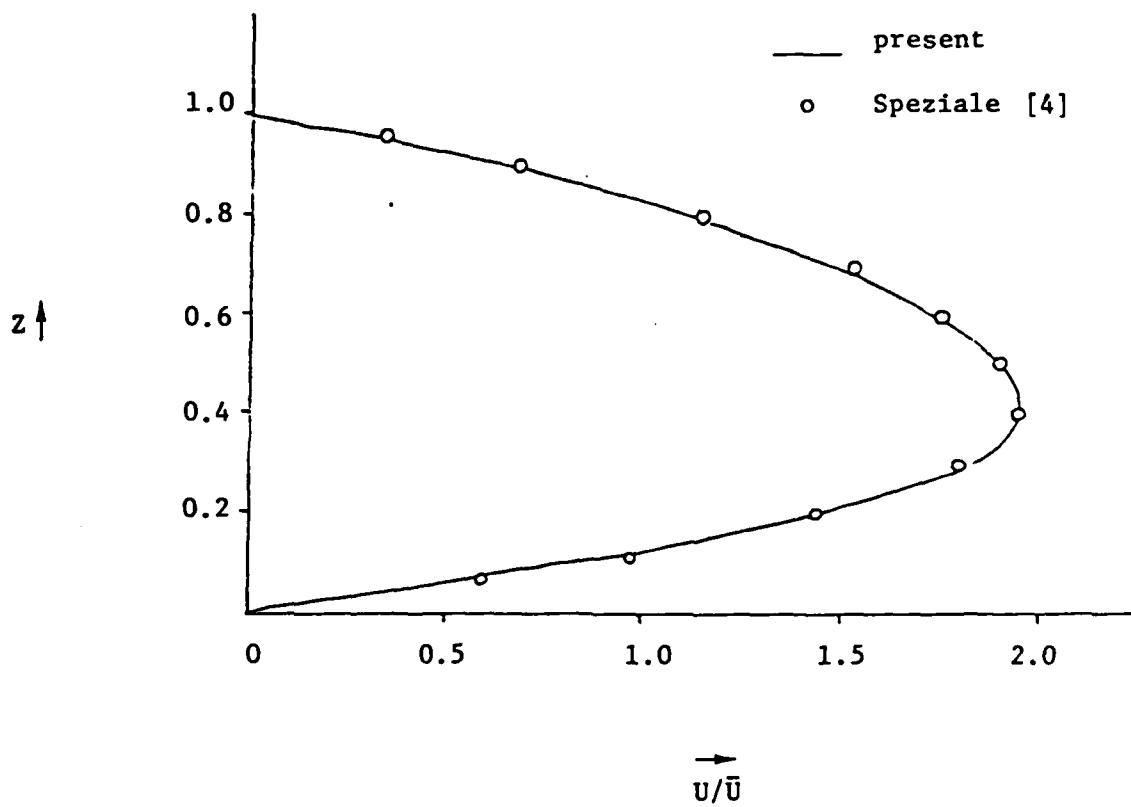Figure 2 – Contour plot of the streamwise velocity;
Re = 235, Ro = 50.5.

Figure 3 – Streamwise velocity profile along the centerline of the duct; Re = 235, Ro = 50.5.

the centerline is clearly evident from the plot and is predicted by the present computations in comparison with the computations of Speziale. The cause of the distortion of the streamwise velocity profile is the secondary velocity field developed in the duct from the effects of the Coriolis force. This secondary velocity is shown as a vector plot in Figure 4. Although the secondary velocity field is weak, the secondary flow vortex is evident.

A second set of computations are carried out at a Reynolds number of 86 and a Rossby number of 1.85. This Rossby number corresponds to a case of strong rotation effects in the duct. Figure 5 shows a contour plot of the fully-developed streamwise velocity field. The shift of the velocity contours away from the centerline is larger and more distinct than in the previous case. The peak streamwise velocity in the duct is lower than the previous case corresponding to a larger degree of flattening of the velocity profiles due to rotation. Figure 6 shows a vector plot of the secondary velocity field. The secondary velocities are much larger than in the previous case and the secondary flow vortex is stronger. Correspondingly, the distortions of the streamwise velocity profiles are larger than in the previous case. Secondary velocities as large as 17% of the peak streamwise velocity are generated in the duct. Figure 7 shows a plot of the computed streamwise pressure gradient along the length of the duct together with a plot of the centrifugal force and the streamwise reduced pressure gradient. The reduced pressure is the difference between the static pressure and the stress due to the centrifugal force and can be construed as the effective pressure in the flow field in a rotating flow. In Figure 7, the rapidly increasing centrifugal force along the length of the duct due to rotation is matched by increasing static pressure in the duct. However, after the initial entrance region of the duct, the streamwise reduced pressure gradient remains constant and is a favorable pressure gradient. The reduced pressure gradient balances the viscous shear stress developed at the walls of the duct in the fully-developed region of the flow field. This is similar to balance of the streamwise pressure gradient and the wall shear stress in the case of a non-rotating duct.

Although these test cases focus upon rotating internal flow, they represent necessary test cases in the development and verification of a rotating flow capability. As can be seen from Figure 3, this capability appears to be confirmed through comparison with an alternate calculation. The remaining results show the expected physical phenomena.
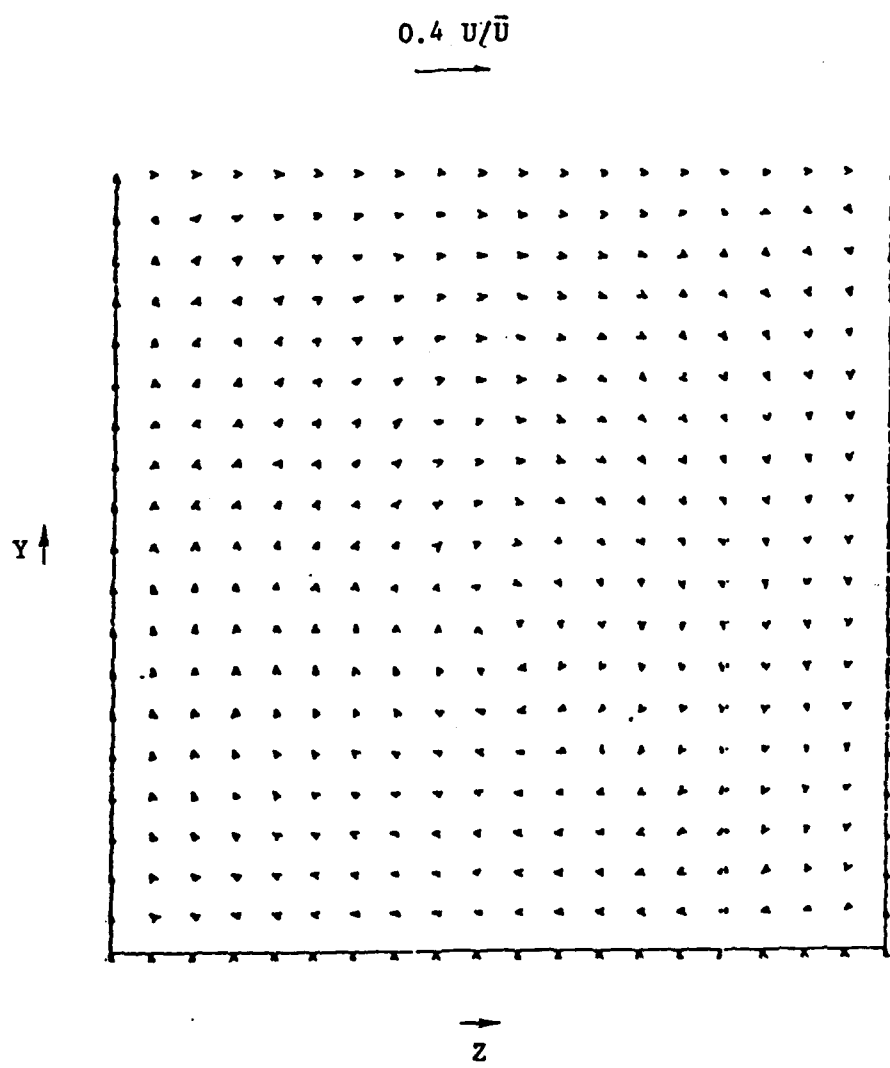
15

0.4 $U/\bar{U}$

Y ↑

Z

Figure 4 - Vector plot of the secondary velocity field;
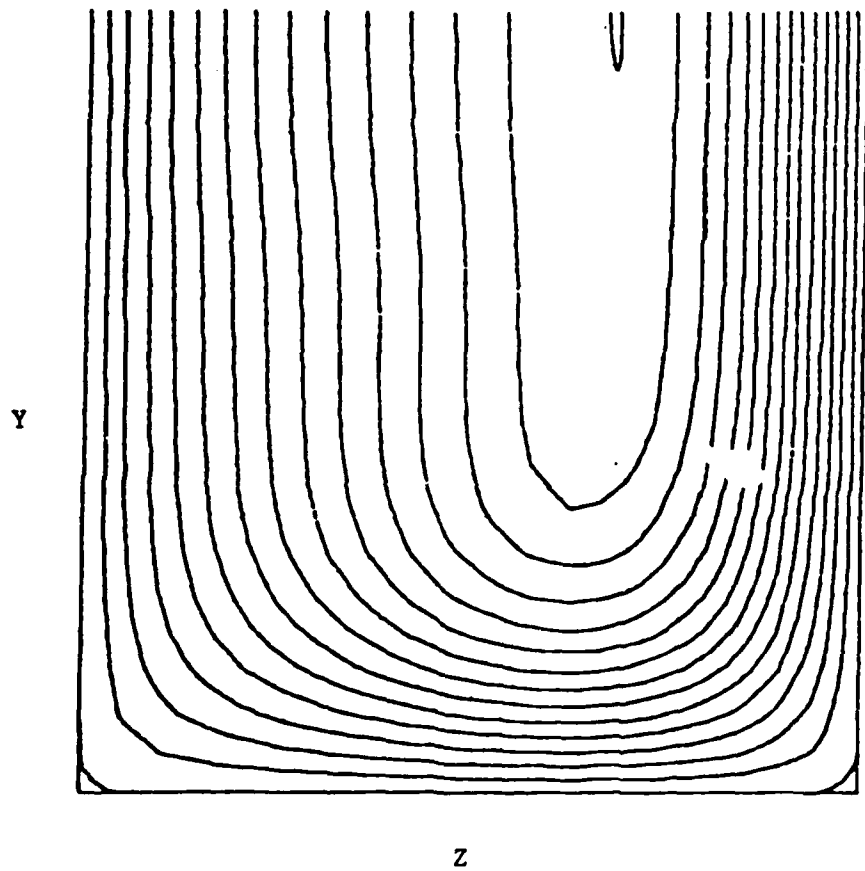Re = 235, Ro = 50.5.

16

Maximum Velocity (U/$\bar{U}$) = 1.870

Y

Z

Figure 5 – Contour plot of the streamwise velocity;
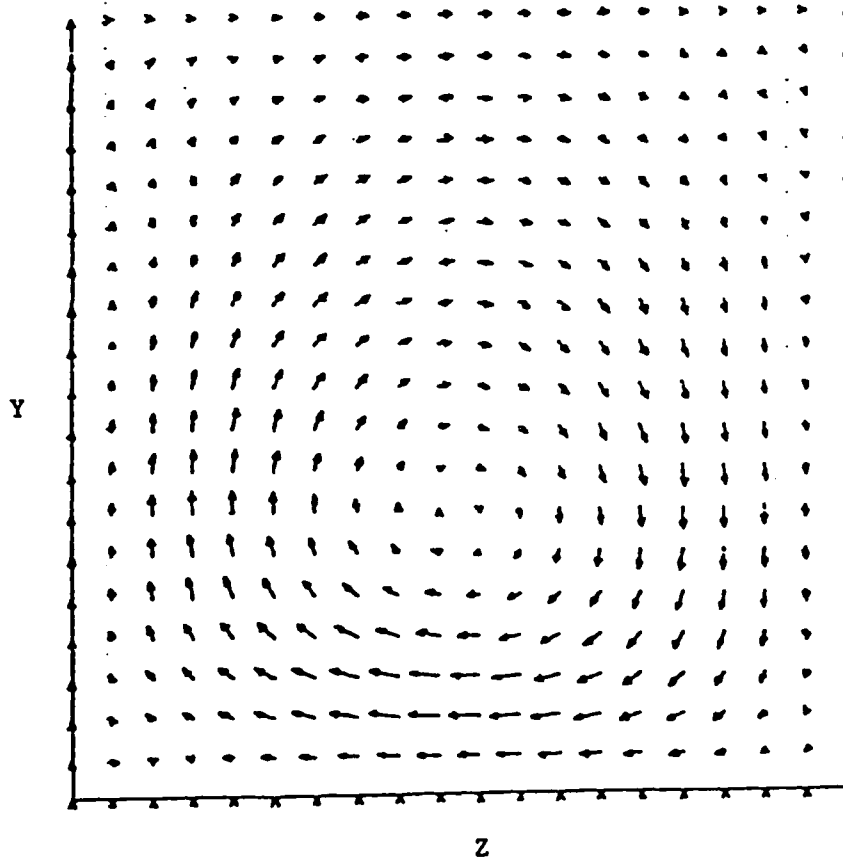Re = 86, Ro = 1.85.

0.4 U/Ū

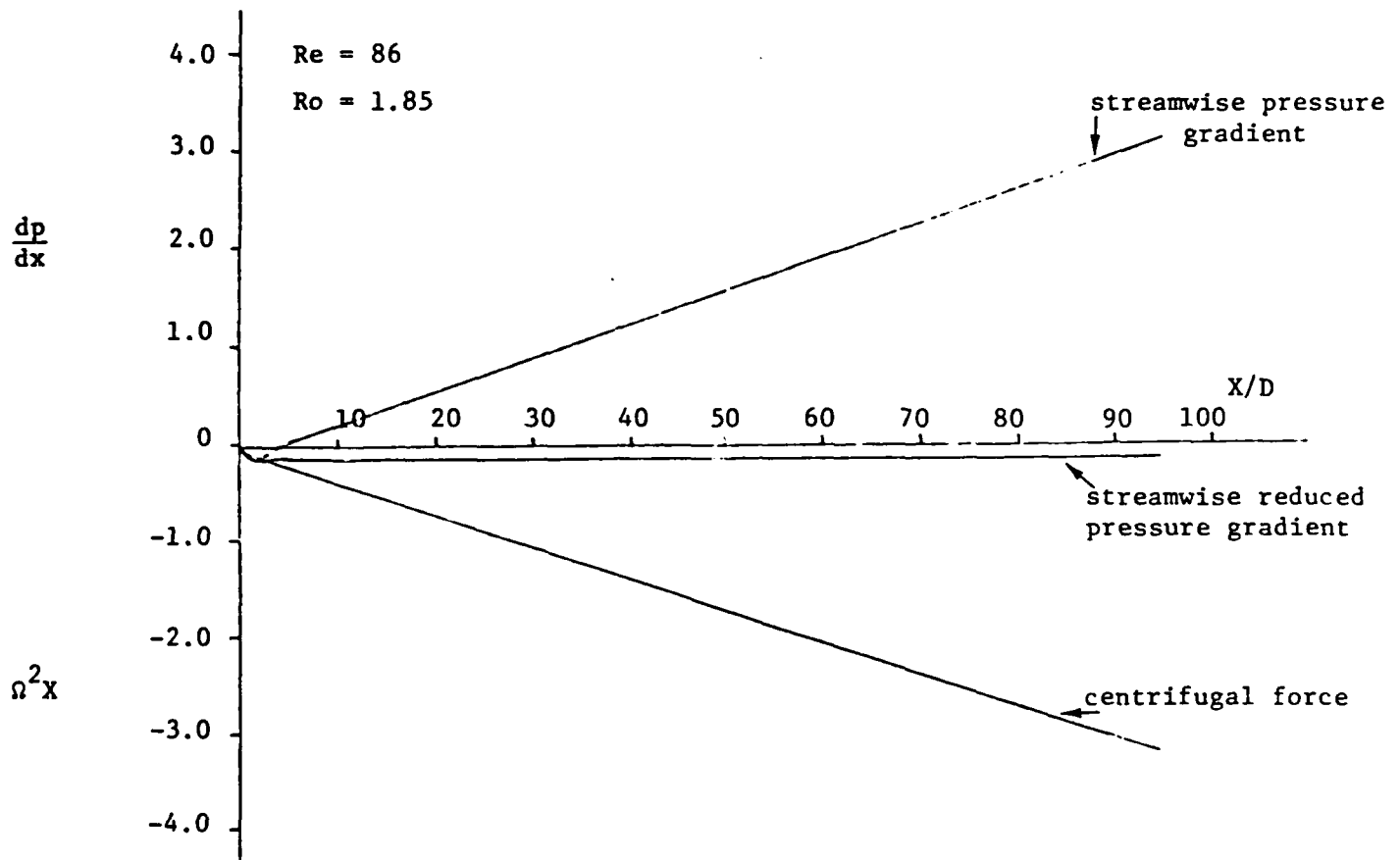Figure 6 – Vector plot of the secondary velocity field;
Re = 86, Ro = 1.85.

18

Figure 7 – Axial variation of the streamwise pressure gradient, centrifugal force, and the streamwise reduced pressure gradient.

3.2 Computation of Flow Over a Circular (Rounded) Cross Section Tip

The next step was computation of a flow field that contained the flow processes in the generation of the tip vortex. At this point in the computations and to better understand the flow processes; the isolation of the effects of complex geometry, rotation, and the effects of the leading and trailing edges was appropriate. For this purpose, the flow over a blade tip with a circular cross section and constant blade thickness was chosen as a test case.

A test case was run for the laminar flow over a circular tip, described above, at an angle of attack of 6°. The Reynolds number for the flow was set at 800 based on the thickness of the tip (d). The viscous dissipation at this Reynolds number is typical of levels of maximum dissipation in a turbulent flow field. An initial boundary layer thickness of 20% of the thickness of the tip was used to construct the initial axial velocity profile. Cross flow velocities and a vorticity field compatible with the initial axial velocity profile were computed by the starting procedure in the computer code. Figure 8 shows the flow configuration of the test case. A computational grid of 40 circumferential points and 25 radial points was used in the calculations. Radial clustering of the grid points was used to resolve the flow in the shear layer.

Figure 9 shows results of the computation at a station 5.20d downstream from the initial station. Figure 9(a) shows a contour plot of the axial velocity (velocity component parallel to the x-axis). The initial stage of the development of the tip vortex is evident in this figure. The convection of low momentum fluid, in the shear layer, from the pressure side to the suction side results in a thickening of the shear layer on the suction side and a thinning of shear layer on the pressure side. A small distortion of the velocity contours on the suction side is indicative of the weak vortex in the region. The transport of low momentum fluid from the pressure side to the suction side is more clearly seen in the contour plot of the streamwise vorticity field shown in Figure 9(b). The cross flow velocity across the tip transports vorticity from regions of high vorticity in the thin shear layers on the pressure side to the suction side causing an accumulation of low momentum fluid on the suction side. The low momentum fluid rolls up to form the tip vortex as it is convected away by the axial velocity. Figure 9(c)
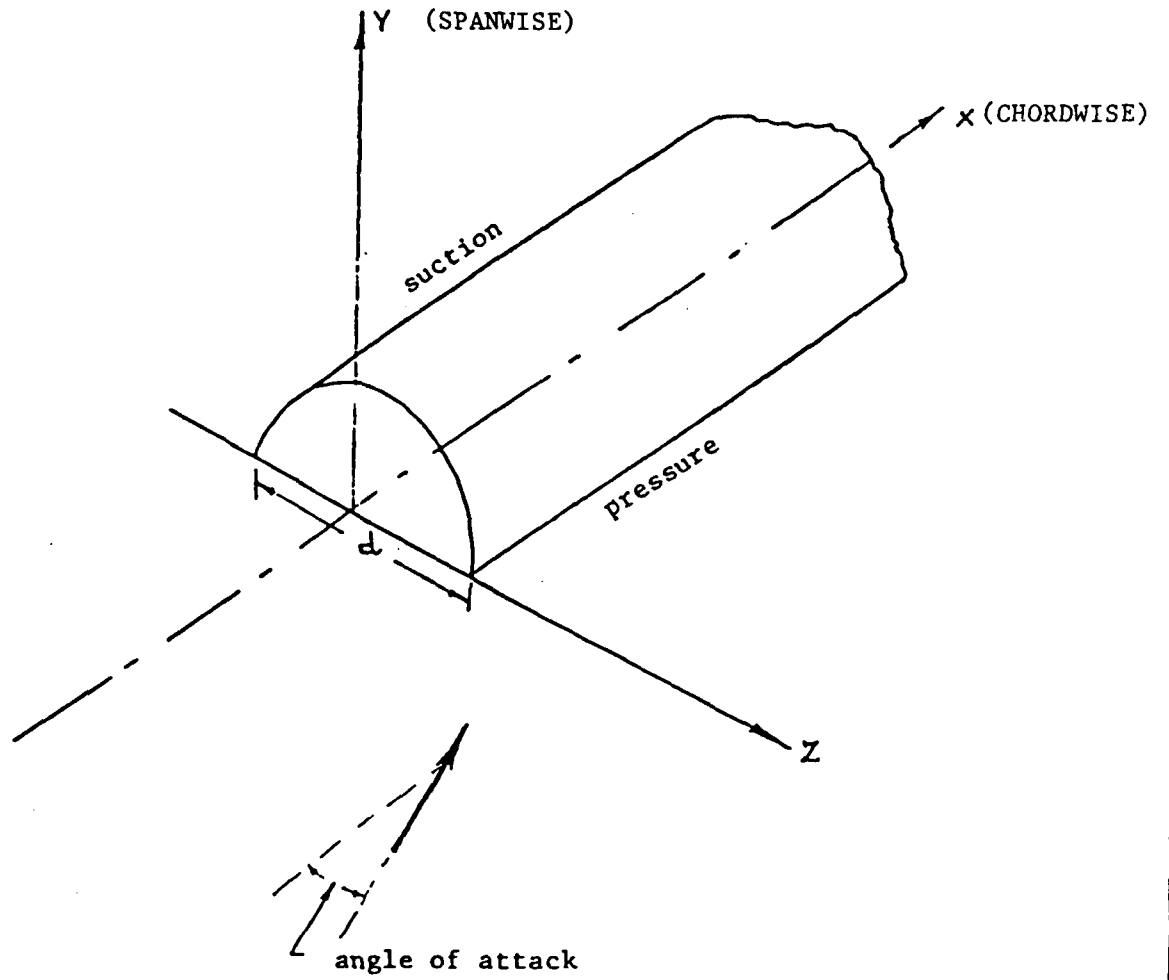
20

Figure 8   Flow Over a Circular Tip

21

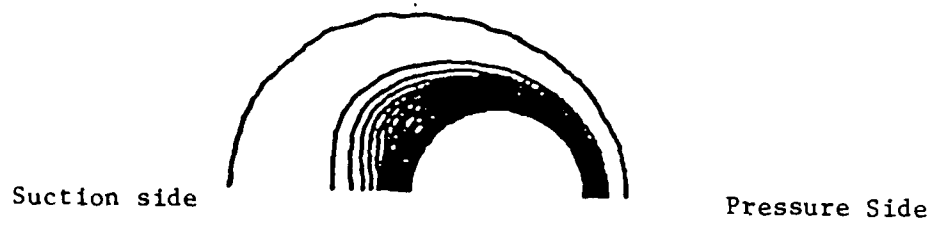Suction side   Pressure Side

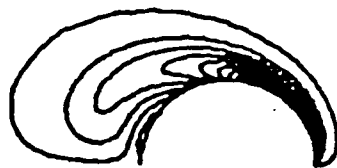Figure 9(a)   Contours of Axial Velocity
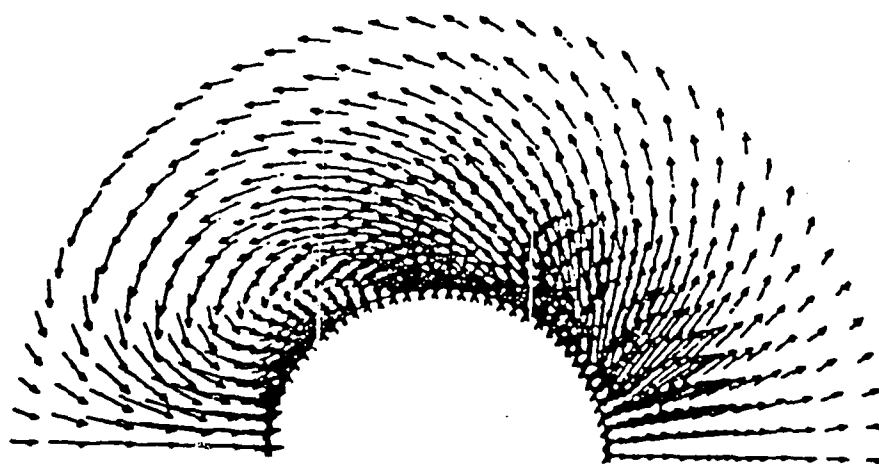
Figure 9(b)   Contours of Streamwise Vorticity

Figure (9c)   Vector Plot of the Cross-Stream Velocity Field (Expanded View)

Figure 9   Flow Field at Axial Station 5.20d

22

shows a vector plot of the transverse velocity components perpendicular to
the free stream velocity. It should be noted that Figure 9(c) shows the
secondary velocity field, the primary velocity is perpendicular to the plane
of the figure. For clarity, the flow field in the vicinity of the tip has
been magnified and the far field flow omitted. The figure shows the
incipient roll up of the flow into the tip vortex. The outward velocities at
the bottom (in the figures) of the pressure surface are due to the
displacement effect of the growth of the shear layer on the tip.

Figure 10 shows the results of the computation at a station 15.70d
downstream from the initial station. Figure 10(a) shows a contour plot of
the axial velocity. The shear layer on the suction side has grown rapidly.
Further, the contours of the axial velocity are distorted by the tip vortex.
The contours of streamwise vorticity (Figure 10(b)) show the extent of the
spread of the vorticity convected to the suction side by the cross-flow
velocities. The large body of low momentum fluid on the suction side has
rolled up into a vortex (Figure 10(c)). The vortex draws fluid into the
bottom (in the figures) of the suction surface that is convected away by the
axial velocity. This process causes the distortions of the axial velocity
contours seen in Figure 10(a). The results show the ability of the PEPSIG
computer code to capture the flow processes in the generation of the tip
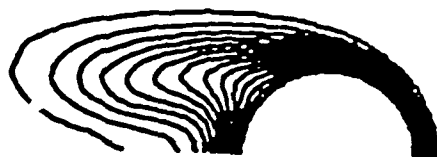vortex.

Figure 10(a) Contours of Axial Velocity

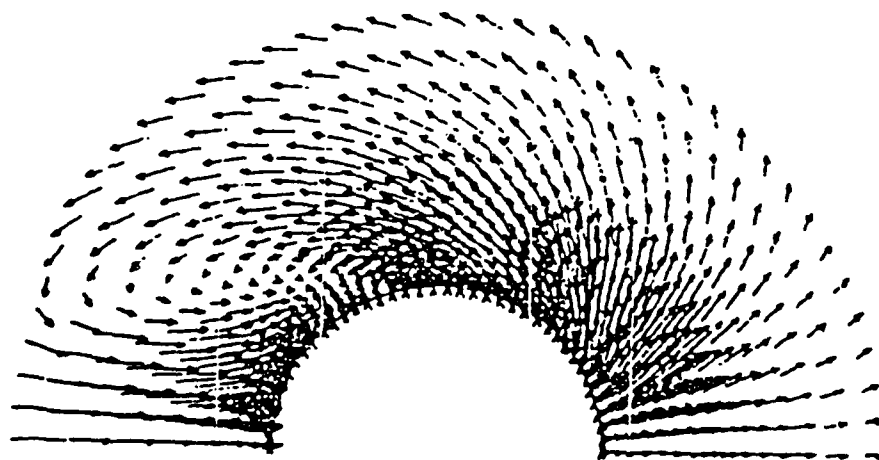Figure 10(b) Contours of Streamwise Vorticity

Figure 10(c) Vector Plot of the Cross-Stream Velocity Field (Expanded View)

Figure 10 Flow Field at Axial Station 15.70d

24

4. COMPUTATION OF THE TIP VORTEX FLOW FIELD

The ingredients for successful computation of the tip vortex generation process for ship propeller blades were formulated and verified in the previous subsections. To demonstrate the capability of the forward marching procedure to compute the tip vortex generation process three test cases were chosen:

(1) Tip vortex flow for a straight blade with rounded tip,

(2) Tip vortex flow for a rotating straight blade with rounded tip,

(3) Tip vortex flow for a rotating twisted blade with rounded tip.

The test cases were chosen for a graded increase in complexity towards the computation of the tip vortex flow for a realistic ship propeller blade. Laminar flow was assumed in all the cases since the qualitative nature of the tip vortex generation process remains the same in laminar and turbulent flow and inclusion of a turbulence model was deemed premature under this feasibility study.

A major portion of the Phase I effort concerned a propeller geometry package. Under Phase I, a geometry package was incorporated into the computer program to describe the propeller tip geometry and generate a suitable computational grid. Figure 11 shows one of the geometries that was used for the propeller tip. The figure shows a constant thickness blade with a rounded tip. Figure 12 shows a cross-section of the propeller tip and the computational grid at a typical streamwise station. The leading edge is upstream of the region shown. The calculation is initiated at a chordwise station on the blade with an assumed velocity profile. A computational grid that wraps around the tip was chosen to provide adequate resolution of the tip region and a smooth grid distributuion. The geometry package has the ability to control grid point distribution in both transverse coordinate directions to resolve regions of high gradients in the flow. Streamwise curvature of the blade and blade twist can also be handled by the geometry subroutines.

4.2 Boundary Conditions for the Tip Vortex Flow Computations

The cross-sectional computation coordinate system, shown in Figure 12, has four boundaries where boundary conditions for the governing equations
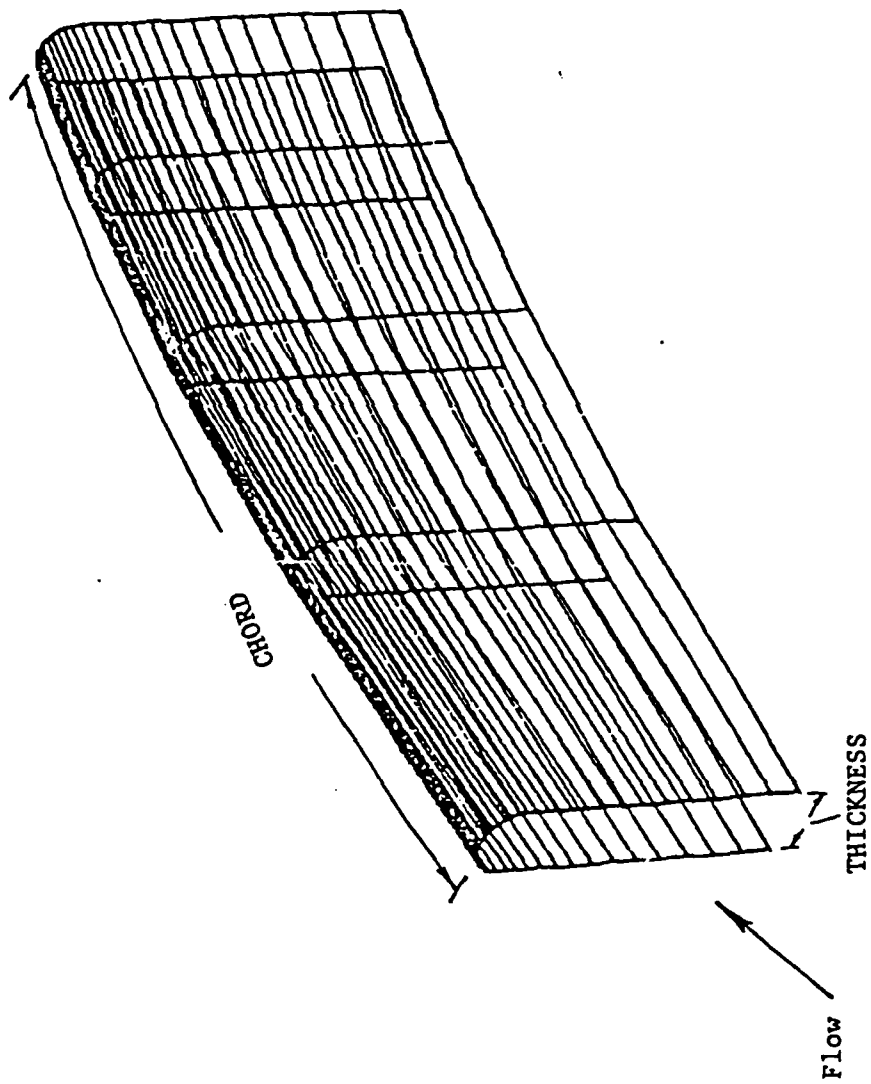
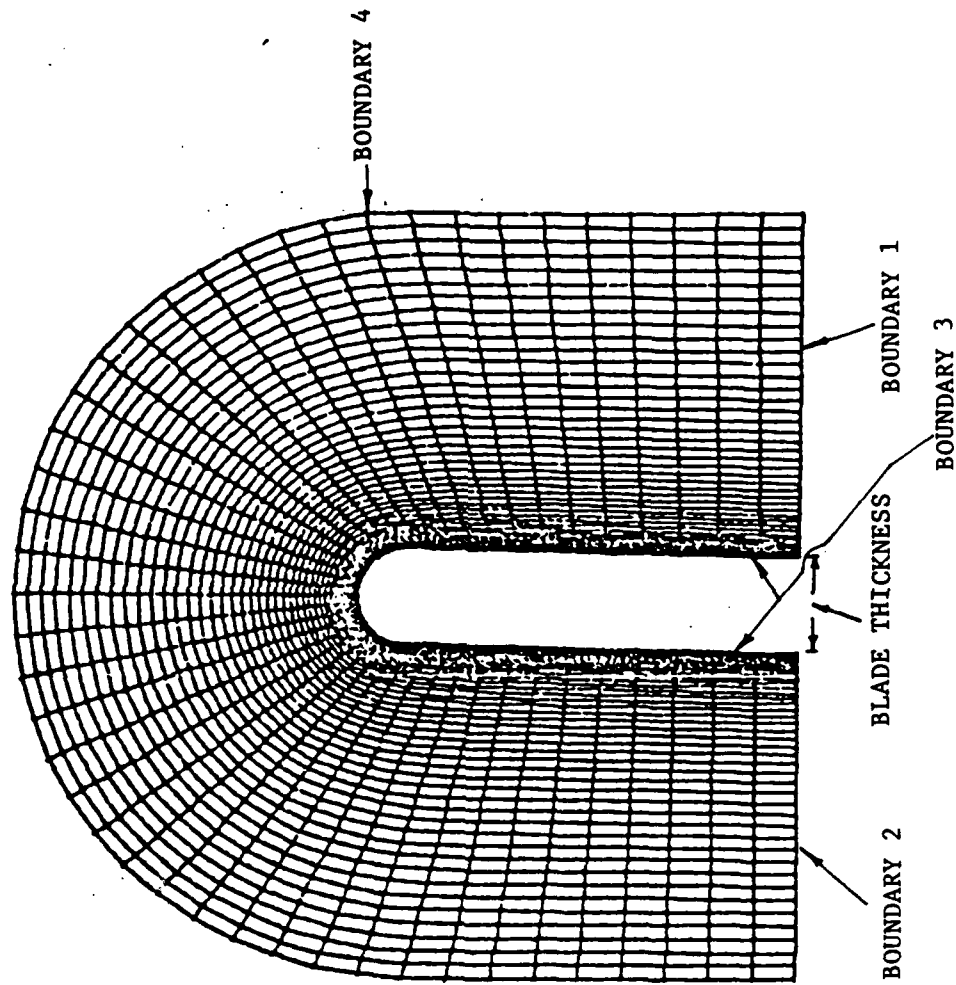Figure 11 - Perspective view of the straight blade.

Figure 12 - Transverse Computation grid at a typical streamwise station.

must be specified. Inboard are boundaries (1) and (2), the blade surface is boundary (3), and the far field is boundary (4). Boundary conditions must be specified for the streamwise velocity in the streamwise momentum equation, for the scalar potential in the scalar potential equation, and for the vector potential and streamwise vorticity in the coupled vector potential-streamwise vorticity equations. The conditions that were specified for the tip vortex flow computations are considered in this section.

The flow at the inboard boundaries (1) and (2) was assumed to be two-dimensional (no spanwise variation) with no flow penetration of the secondary velocity through the boundaries. The normal gradient of the scalar potential was set to zero and the vector potential was set to a constant (normal velocity set to zero). The streamwise vorticity was set to zero as the compatible condition with the vector potential and the streamwise velocity was extrapolated from the interior flow field. The boundary conditions specified on the inboard boundaries are only approximate but were found not to affect the qualitative computed behavior of the tip vortex generation process. Under a contract from the NASA Langley Research Center for the helicopter tip flow field, boundary conditions based on the induced velocity field by the blade are currently being developed. These conditions will be incorporated in future work on the ship propeller tip flow field.

The boundary condition along boundary (3), the blade, was the no-slip condition on a solid surface. To satisfy this condition the normal gradient of the scalar potential (the normal velocity) was set to zero. In the coupled vector potential and vorticity equations the normal component of the rotational velocity was set to zero and the tangential component was set equal and opposite to the tangential component of the velocity generated by the scalar potential. These conditions allowed an implicit specification of the vector potential and the vorticity on the no-slip boundary (as discussed in Section 3). The resultant secondary velocity field satisfies the no-slip conditions on the boundary. The streamwise velocity was also set to zero at the solid boundary.

Far field conditions were specified on boundary (4). The streamwise velocity was extrapolated from the interior flow field. The scalar potential was set to a constant so that the tangential component of the irrotational velocity was zero. This condition allowed outflow through the boundary due to the displacement effect of the boundary layers on the blade. The angle of

28

incidence of the flow specified a component of the transverse velocity on the boundary. The vector potential was obtained by integrating this component of the transverse velocity along the boundary. The streamwise vorticity was set to zero.

4.3 Computation of the Tip Vortex Flow for a Straight Blade with Rounded Tip

A constant thickness blade with a rounded tip was the first test case considered for the tip vortex flow computation. Figure 11 shows a perspective view of the geometry of the blade near the tip. Figure 12 shows the cross-section of the blade tip and the computational grid at a typical streamwise station. The important geometric and flow parameters used in the computation were the following:

Blade thickness (t)	=	1.0
Blade chord	=	20.0t
Reynolds number (based on t)	=	1000.0
Initial boundary layer thickness	=	0.20t
Incidence angle	=	6°

A computational grid of 60 streamwise stations and a 47 x 30 cross-section grid was used. Grid points were clustered in regions of high flow gradients such as near the propeller surface and in the tip region. The computation was started on the blade ($x/t = 0.0$) with the assumed initial boundary layer thickness.

Figure 13 shows the development of the tip vortex computed by the code. The upper half of the figure shows the development of the tip vortex in term of contours of the streamwise velocity while the lower half shows the same development in terms of contours of streamwise vorticity. Computations from five streamwise stations ($x/t = 2.0, 4.0, 7.0, 11.0, 20.0$) were chosen to display the development of the tip vortex. An initial overall view of Figure 13 shows a large scale flow process at the tip of the blade in terms of both the streamwise velocity and streamwise vorticity.
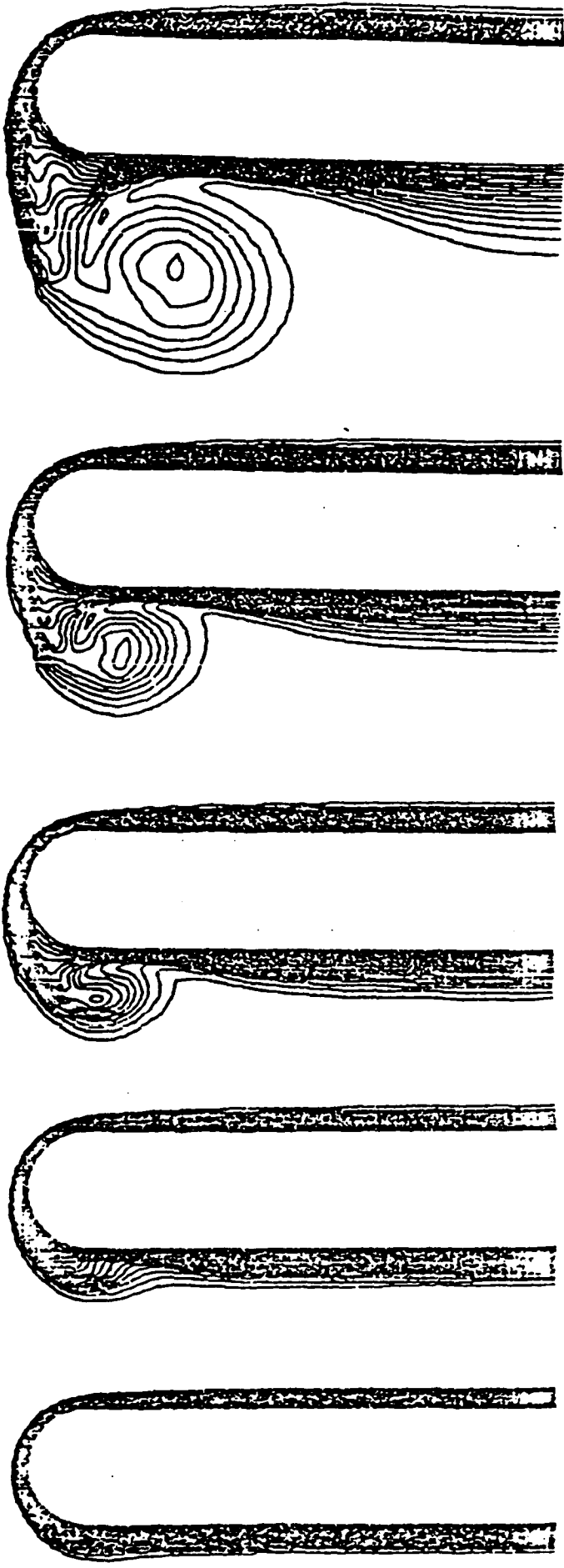
At $x/t = 2.0$ (Figure 13), the streamwise velocity contours show the initial development of the flow. The boundary layer on the suction side of the blade has thickened while the boundary layer on the pressure side remains thin. The thickening of the boundary layer on the suction side is due to the

29

transport of low momentum fluid from the pressure side boundary layer around the tip to the suction side. The same flow process is seen in the streamwise vorticity contours as a transport of vorticity around the tip.

At x/t = 4.0, the tip flow field begins to show the accumulation of low momentum fluid on the suction side of the tip region. This accumulation is characterized by the "bulge" in the streamwise velocity contours representing the region of the low streamwise velocity fluid. The streamwise vorticity contours at this station show the convection of vorticity into this region. Further, the vorticity contours also start to "peel" off the suction surface indicating the initial stages of the roll-up of the low momentum fluid. At x/t = 7.0 and x/t = 11.0, the streamwise velocity contours show the further rapid accumulation of the low momentum fluid in the tip region. The streamwise vorticity contours at these stations show the roll up of the tip flow into the tip vortex. The vorticity contours emanating from the suction surface, visible clearly at x/t = 11.0, are indicative of the outward (toward the tip) transverse velocities in the region due to roll-up of the tip vortex. The results at x/t = 20.0 show the completion of the tip vortex formation. The vortex has separated from the suction surface as it is convected downstream by the streamwise velocity. The vortex is sustained by the continued transport of vorticity from the pressure surface into the vortex core. Also evident from Figure 13 is the inward track of the center of the vortex along the suction side. That, indeed, the flow in the tip region has rolled up into the tip vortex is clearly visualized by a vector plot of the transverse velocity field. Figure 14 shows a vector plot of the transverse velocity field at x/t = 7.0 and x/t = 20.0. The transverse velocity field at x/t = 7.0 clearly shows the initial roll-up of the flow in the tip region into a vortex. The large transverse velocities (about 30% of the free stream velocity) around the tip that convect the low momentum fluid from the pressure side to the suction side are also seen. The transverse velocity field at x/t = 20.0 shows the strong tip vortex on the suction side. The inward track of the center of vortex along the suction side is also seen in the two vector plots.

Figures 13 and 14 clearly show the development of the tip vortex generation process. It should be noted that this process has been calculated from a set of three-dimensional, viscous flow equations which have a no-slip condition at the propeller blade surface. The vortex generation and roll-up
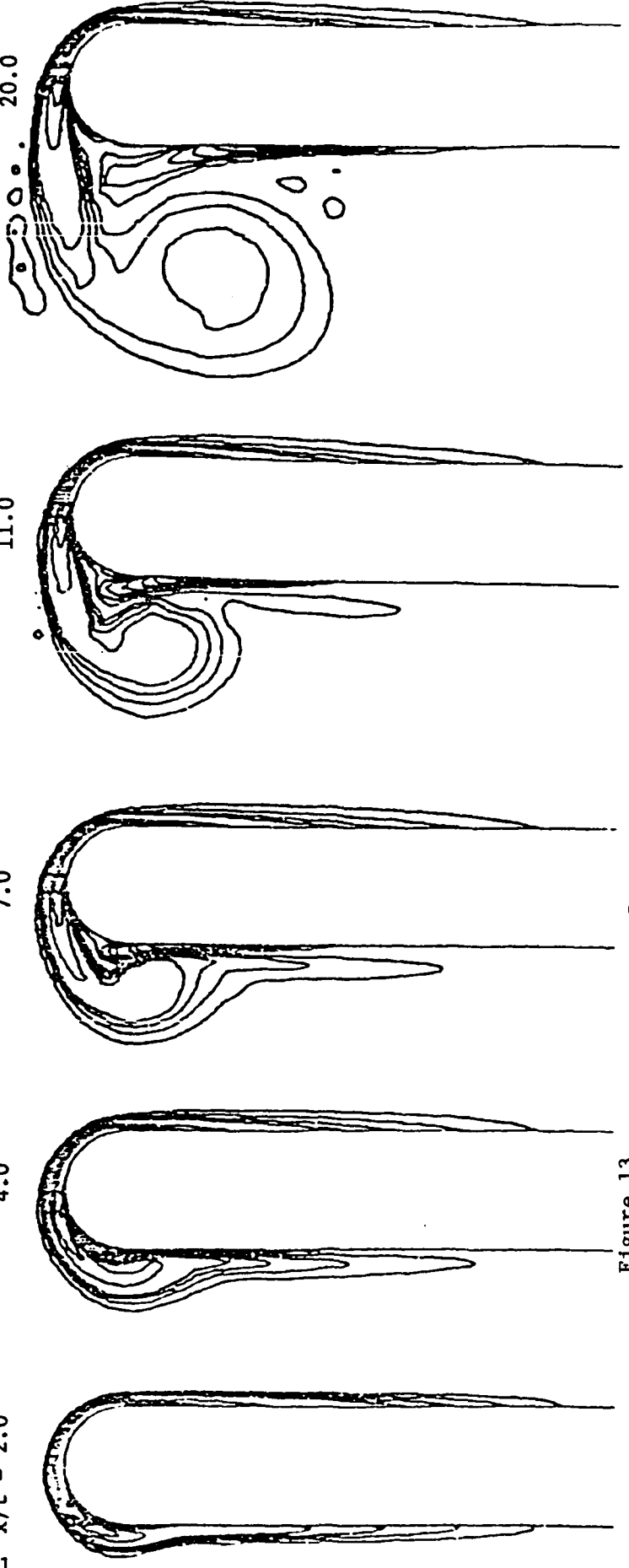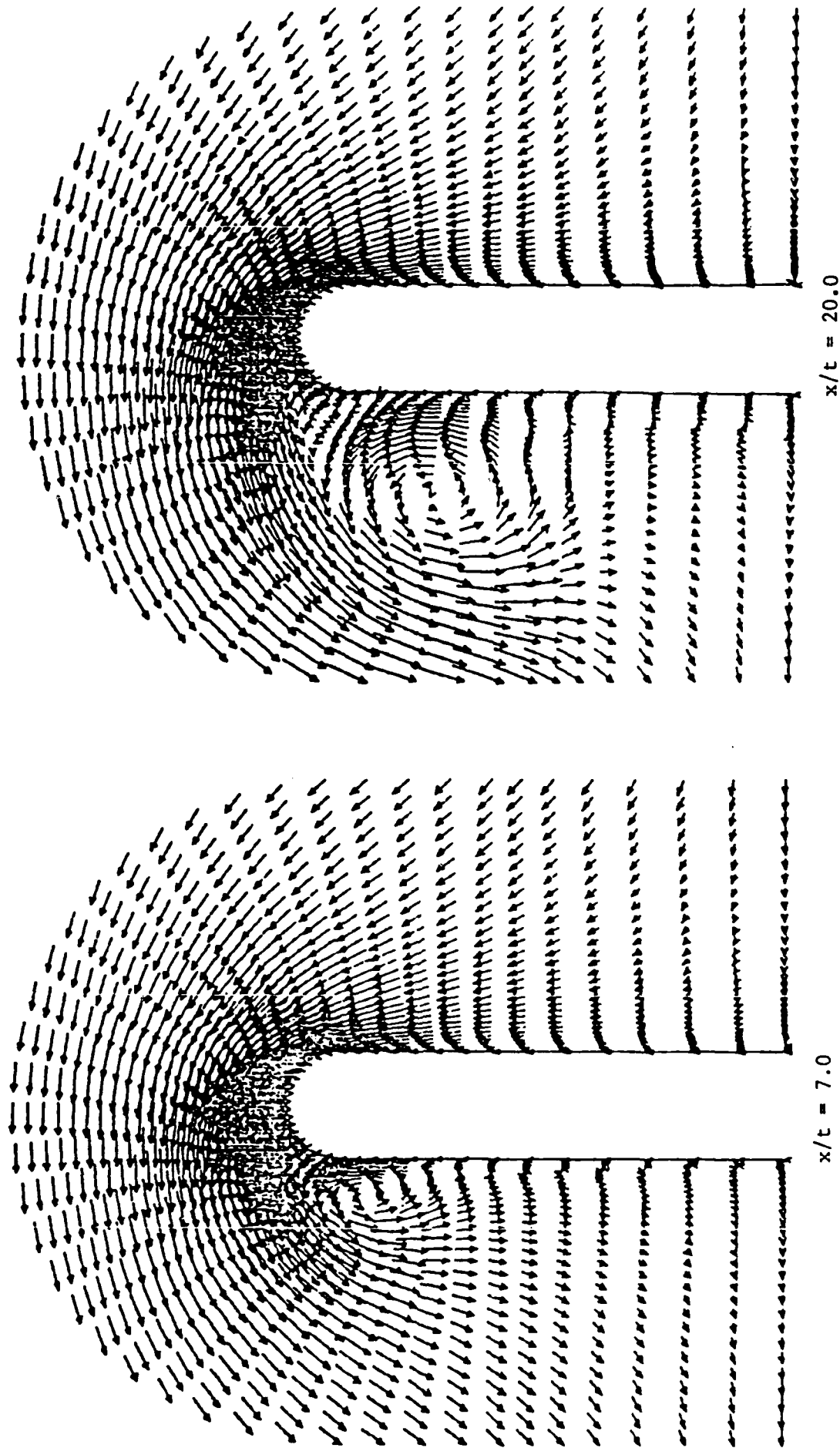
30

Streamwise Velocity

Streamwise Vorticity

x/t = 2.0   4.0   7.0   11.0   20.0

31

Straight blade - no rotation

Figure 13

x/t = 20.0

x/t = 7.0

Straight blade – no rotation

Transverse Velocity

Figure 14

32

is a result of the secondary flow separation, and the computed results obtained are in excellent qualitative agreement with experimentally observed physical processes (Refs. 6 - 8). The calculations clearly show that the tip vortex problem can be analyzed from a consideration of the basic physical phenomena without resorting to empirical models.

4.4 Computation of the Tip Vortex Flow for a Rotating Straight Blade with Rounded Tip

As the second test case in the computation of the tip vortex generation process, the straight blade described in the previous section (section 4.3) was rotated so as to provide an advance ratio of 1.0. The remaining flow and geometric parameters were retained from the previous test case.

Blade Thickness	(t) =	1.0
Blade Chord	=	20.0t
Reynolds Number (based on t)	=	1000.0
Initial Boundary Layer Thickness	=	0.20t
Incidence Angle	=	6°
Advance Ratio	=	1.0

A computational grid of 60 streamwise stations and a 47 x40 cross-section grid was used in the computations. As before, grid points were clustered in regions where high flow gradients were anticipated.

Figure 15 shows the development of the tip vortex computed by the PEPSIG code for the rotating blade. The figure is formatted in the same manner as Figure 13 for the stationary blade. The upper half of the figure shows the development of the tip vortex in terms of contours of the streamwise velocity while the lower half shows the same development in terms of contours of streamwise vorticity. A comparison of Figure 15 with Figure 13 for the stationary case shows the same basic flow mechanisms that result in the generation of the tip vortex. These mechanisms are the transport of low momentum fluid from the pressure side boundary layer to the suction side by the transverse velocity, the accumulation of this low momentum fluid on the suction side of the tip region, and the roll-up of this accumulated fluid into the tip vortex. The differences between the rotating and non-rotating cases are in a matter of the details of the flow structure. These differences will be discussed in this section. A vector plot of the

33

transverse velocity field at two streamwise stations are shown in Figure 16. As in the stationary case, the vector plot shows a clear visualization of the tip vortex. The vector plot at $x/t = 7.0$ shows the early development of the tip vortex while the plot at $x/t = 20.0$ shows the developed tip vortex on the suction side of the tip region.

The differences in the tip vortex flow field between the stationary and rotating blade test cases can be seen by comparing Figures 13 and 15. From an overall point of view, the location of the tip vortex for the rotating blade is higher than the stationary blade. This difference is due to the fact that low streamwise velocity regions in the vortex are regions of higher absolute tangential velocity in the rotating blade. The corresponding increase in the centrifugal force keeps the vortex at a higher location for the rotating blade. In a similar manner, the increase in the absolute tangential velocity in the boundary layers on the suction and pressure surfaces and the corresponding increase in the centrifugal forces that is not balanced by the pressure forces imposed from the outer flow results in outward flow in the boundary layers. This outward flow changes the streamwise vorticity distribution in the vicinity of the blade surfaces. The outward flow in the boundary layers is clearly seen in the vector plot of the transverse velocities near the blade surfaces (Figure 16, $x/t = 20.0$).

4.5 Computation of the Tip Vortex Flow for a Rotating Twisted Blade with Rounded Tip

As a final test case to demonstrate the capability of the forward marching procedure to compute the tip vortex generation process in ship propellers, a computation was carried out of the tip flow field for a rotating twisted blade. The twisted blade geometry was chosen to demonstrate the capability of the forward marching procedure and the geometry package to handle the complex blade shapes typical of a ship propeller. For the purposes of the demonstration computation, the blade twist was specified such that all radial sections of the blade maintained a constant angle of incidence with respect to the incoming flow. The remaining flow and geometry parameters were retained from the previous two test cases.
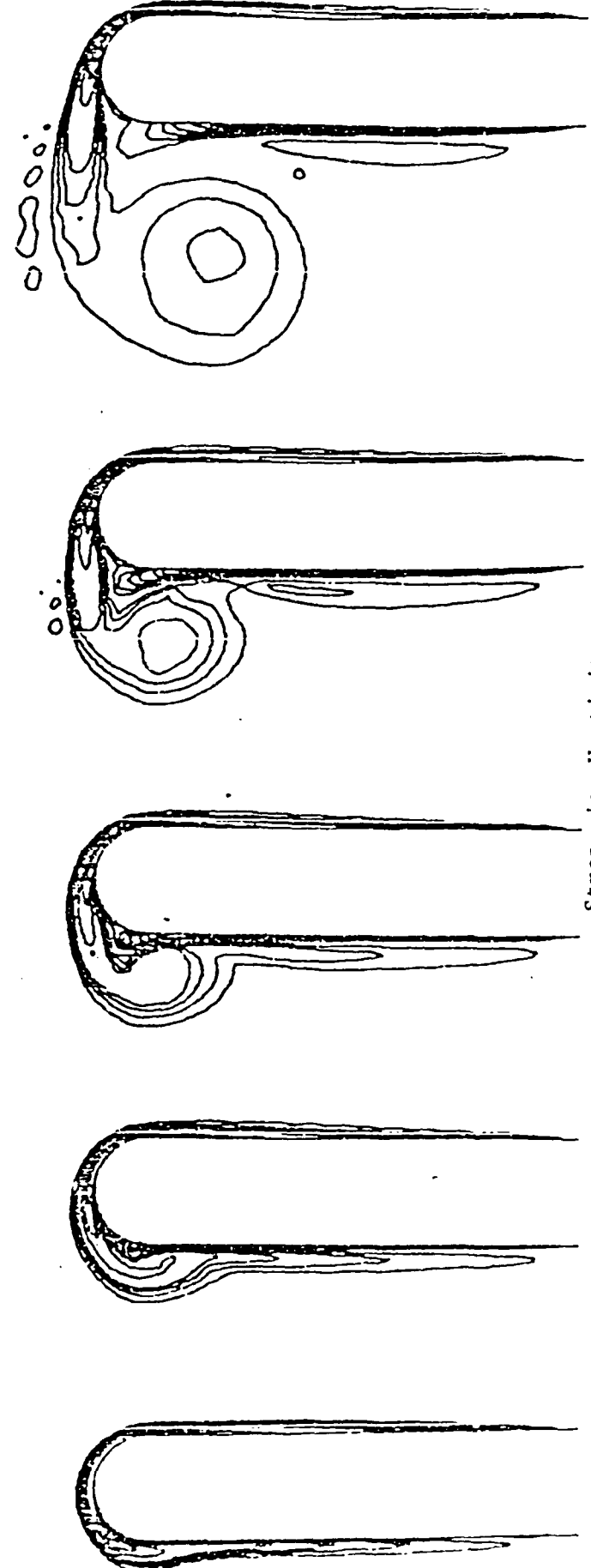
Streamwise Velocity
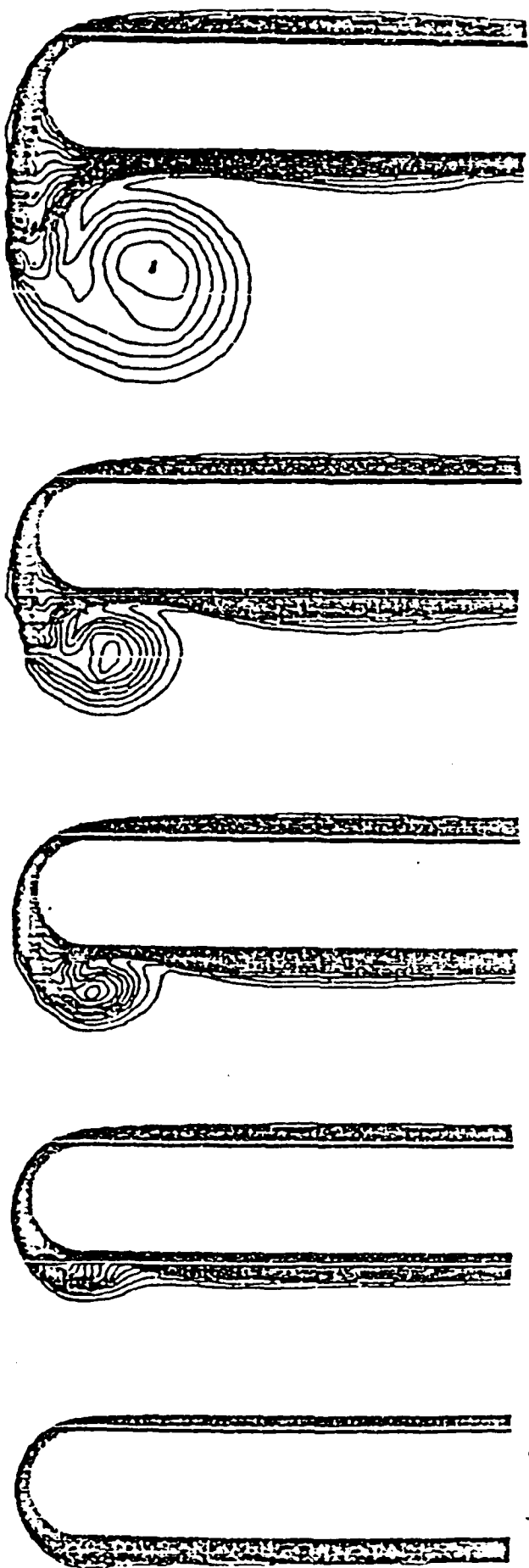
Streamwise Vorticity

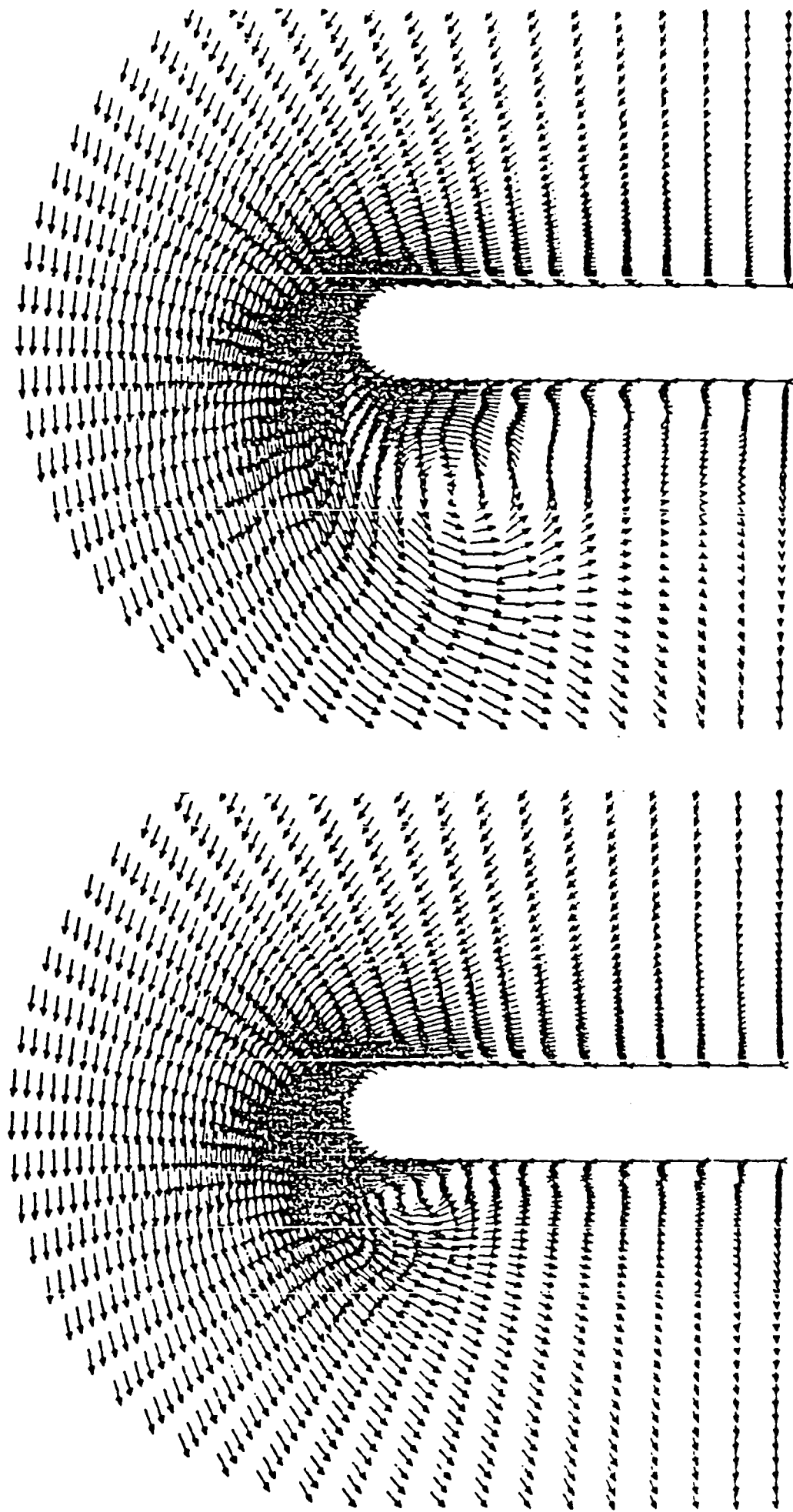Straight blade - rotation

Figure 15

35

x/t = 20.0

Straight blade - rotation

Transverse Velocity

x/t = 7.0

Figure 16

36

Blade thickness (t)		=	1.0
Blade chord		=	20.0t
Reynolds number (based on t)		=	1000.0
Initial boundary layer thickness		=	0.20t
Incidence angle		=	6°
Advance ratio		=	1.0

Geometric twist specified to maintain constant
angle of incidence at all radial blade sections

Perspective views of the twisted blade are shown in Figure 17. A
computational grid of 60 streamwise stations and a 47 x 40 cross-section grid
was used in the computations. Figure 18 shows the computational grid at two
streamwise stations (x/t = 1.0, 20.0). The change in the lean of the blade
along the chord due to blade twist can be seen from this figure. The
geometry package adjusts the grid distribution automatically at each
cross-section to compensate for the blade twist. This capability in the
geometry package can be seen in the computation grid generated at x/t = 1.0
and x/t = 20.0 in Figure 18.

Figures 19, 20 and 21 show the generation of the tip vortex computed for
the rotating twisted blade. Figure 19 shows the initial development of the
flow field. The computation shows the initial transport of low momentum
fluid from the pressure side to the suction side as in the previous test
case. The transverse velocity field is a potential flow like field around
the tip. As in the previous test cases, Figures 20 and 21 show the
accumulation of low momentum fluid on the suction side of the tip region, and
the roll-up of the fluid into the tip vortex. The outward flow in the
boundary layers due to rotation can also be seen in the vector plot of the
transverse velocity field in Figure 21. The change in the lean of the blade
along the blade chord due to blade twist can be seen from the Figures 19, 20
and 21.

With the solution of the velocity field at each streamwise station, it
is possible to compute the transverse pressure field associated with the
generated transverse velocity field. Figure 22 shows a contour plot of the
computed transverse pressure field at x/t = 2.0 and x/t = 4.0. At x/t = 2.0,
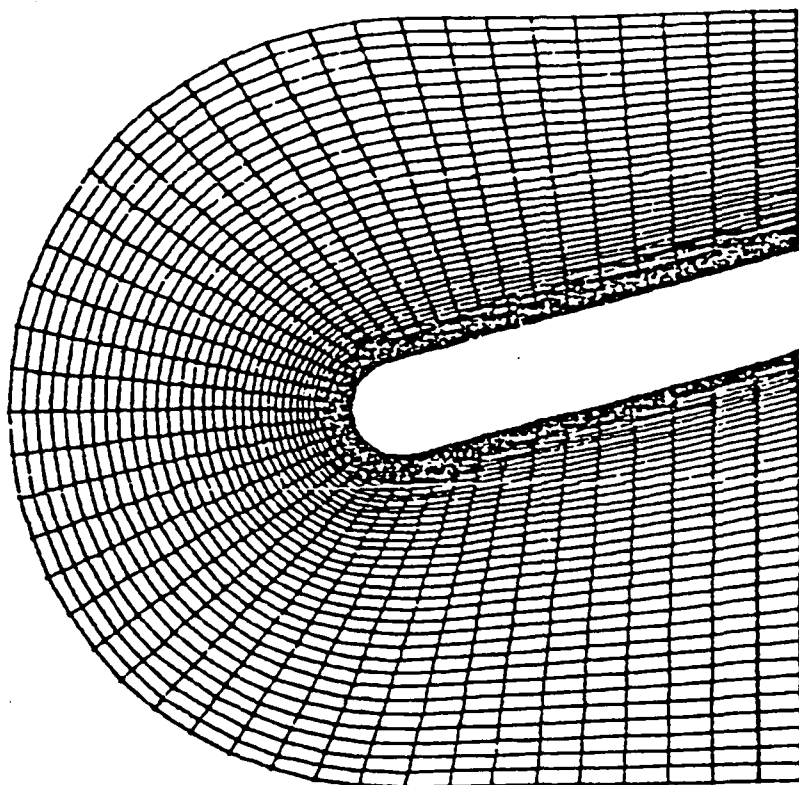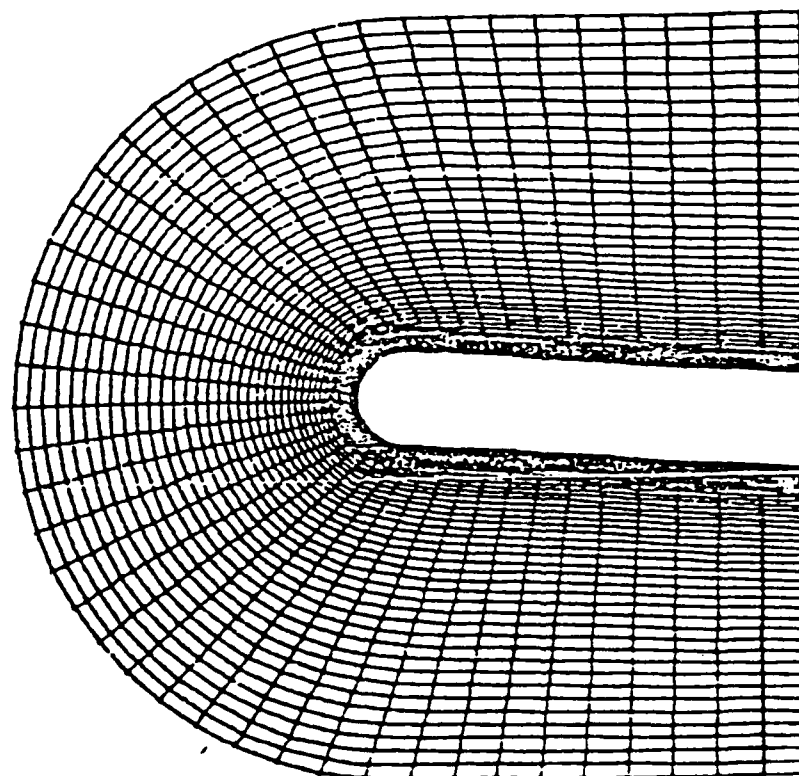the pressure contours show a drop in the pressure as the flow accelerates

37
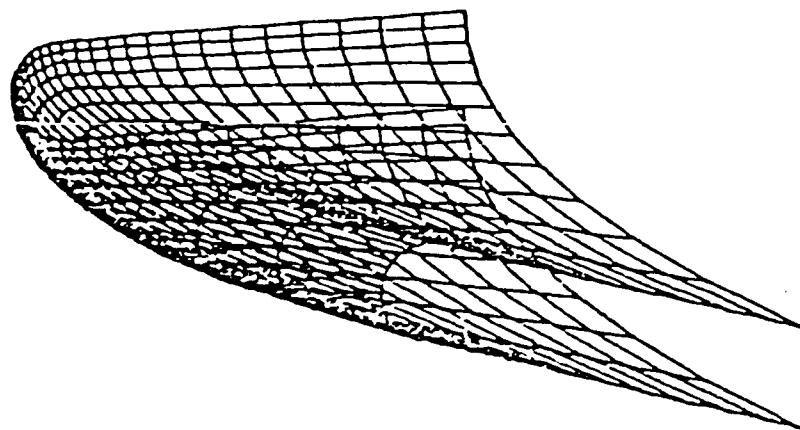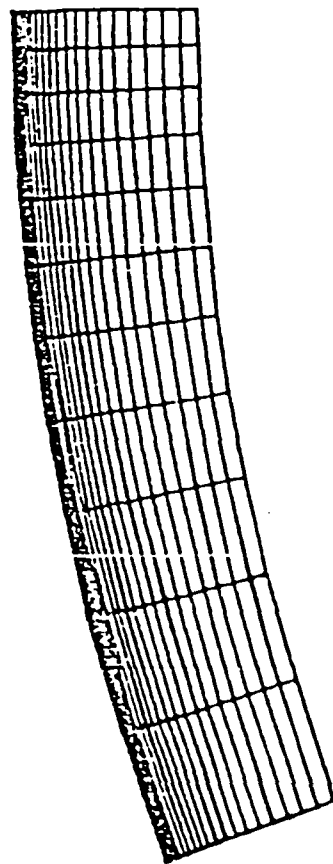
Flow

SIDE VIEW

FRONT VIEW

Figure 17 - Perspective views of the twisted blade
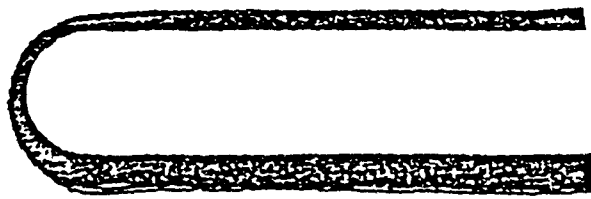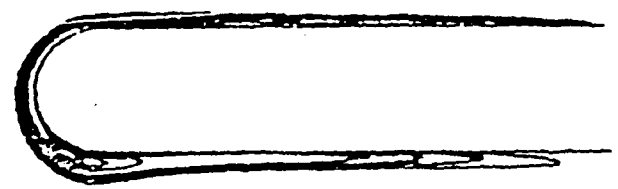
38

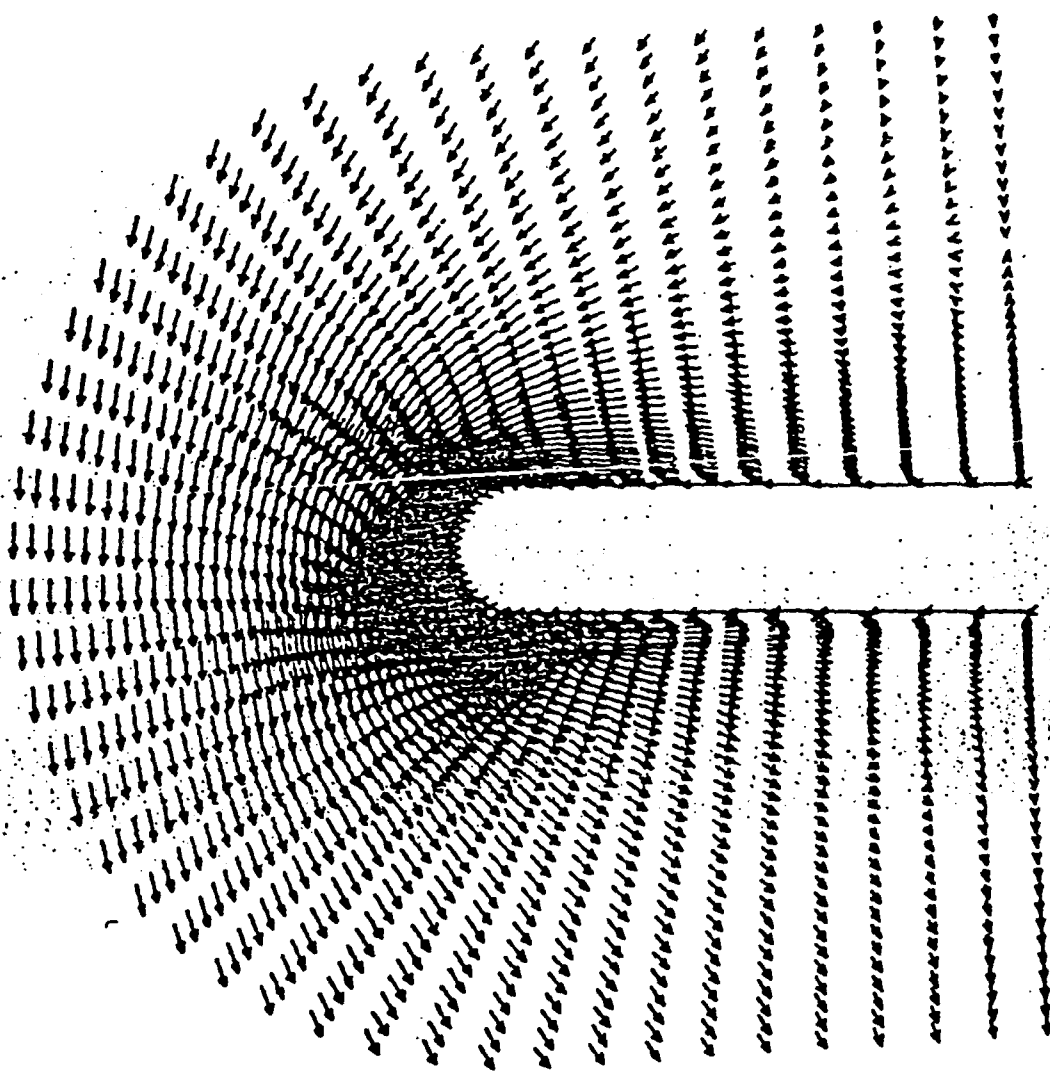$x/t = 20.0$

$x/ = 1.0$

Figure 18 - Computation grid for the twisted blade (front view).
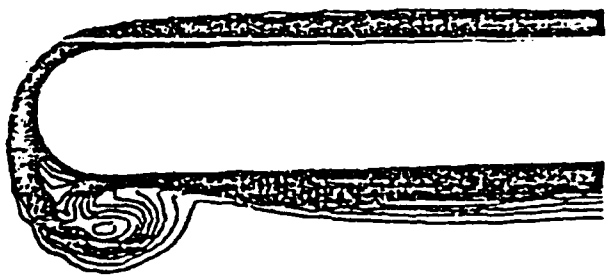
39

Transverse Velocity

Streamwise
Velocity

Streamwise
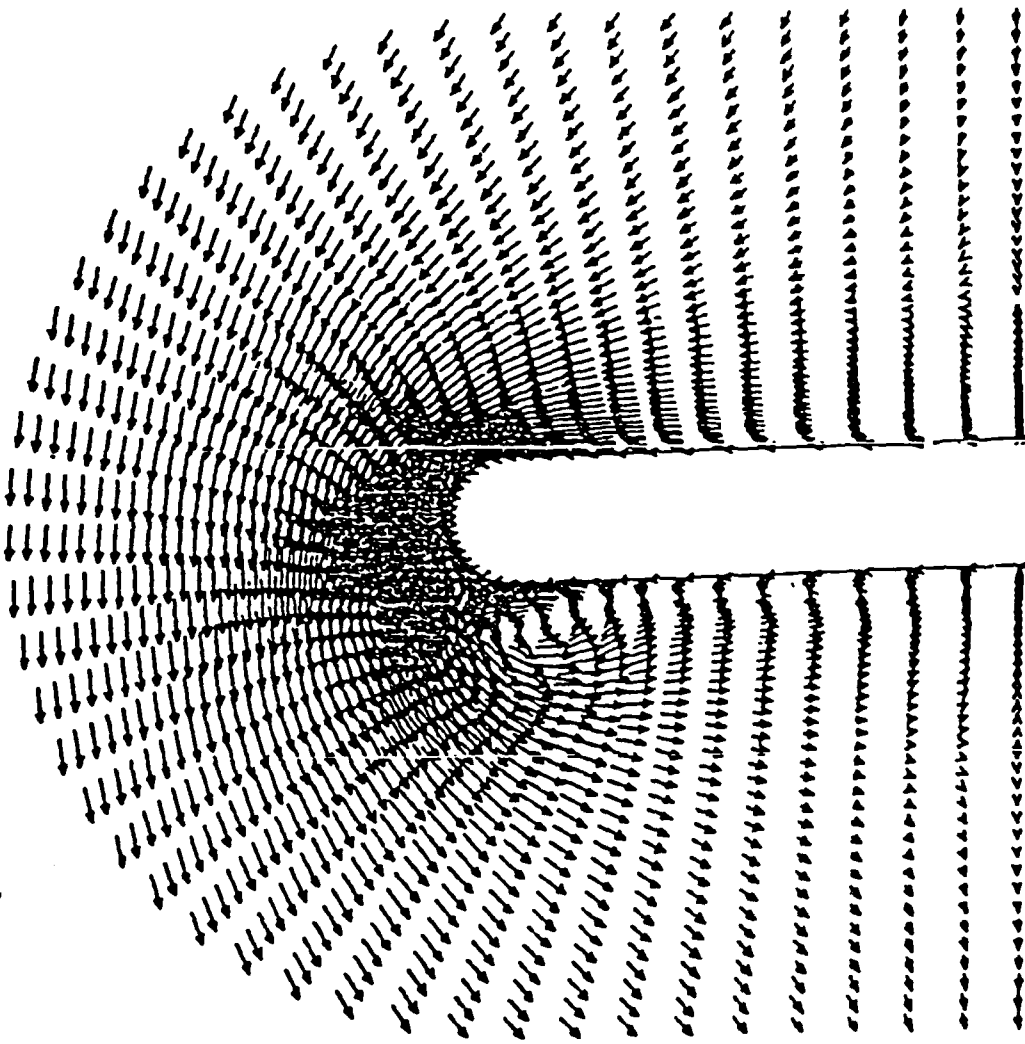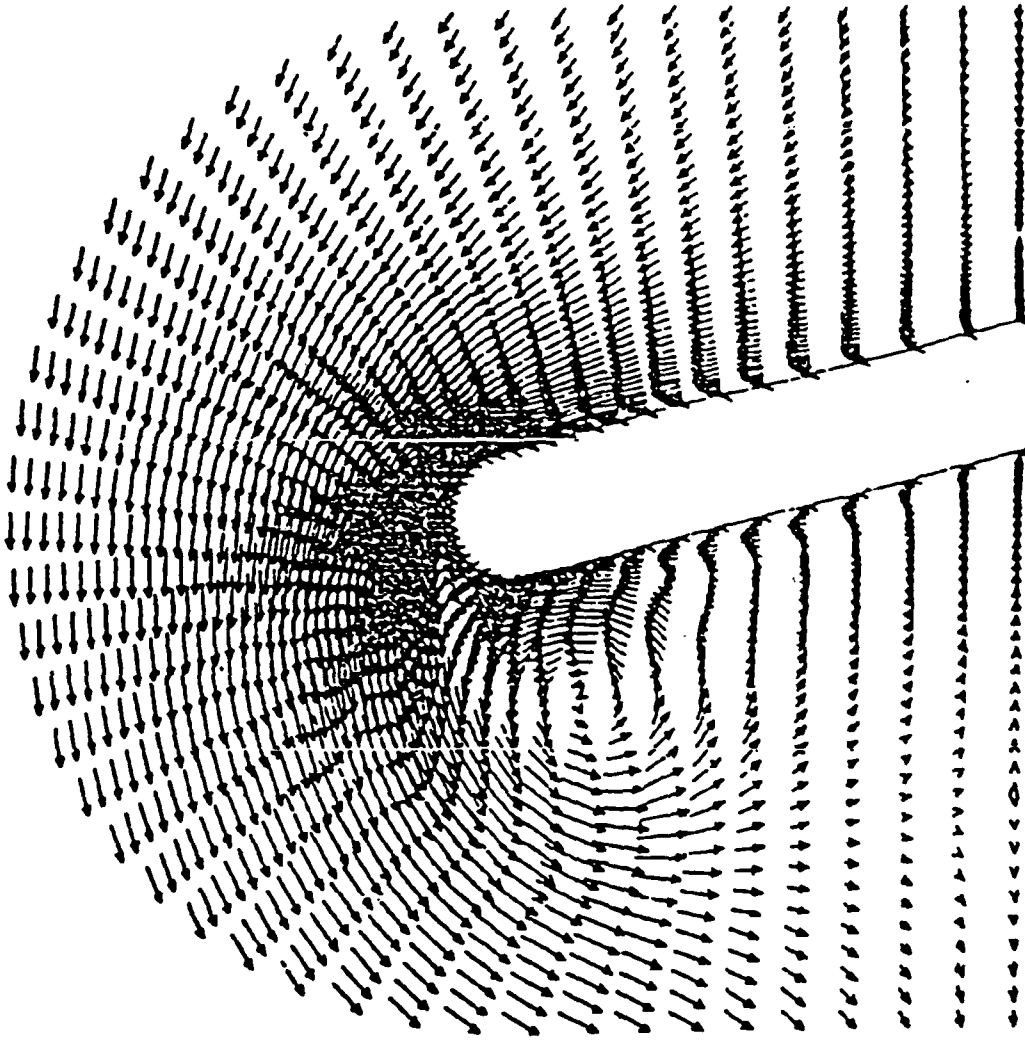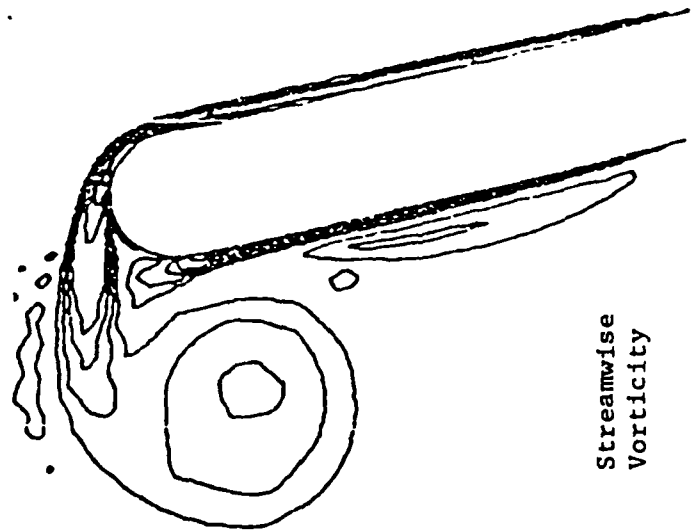Vorticity

Figure 19 - Streamwise Station x/t = 2.0

Twisted blade - rotation

40

Transverse Velocity
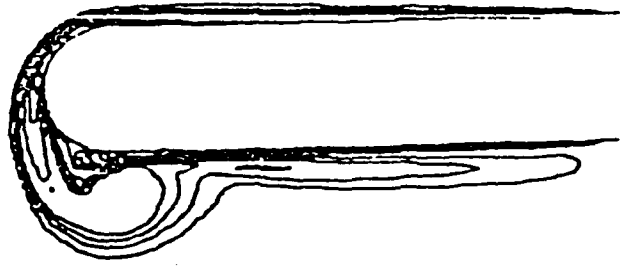
Streamwise Velocity

Streamwise Vorticity

Figure 20 - Streamwise station x/t = 7.0

Twisted blade - rotation

41

Transverse Velocity
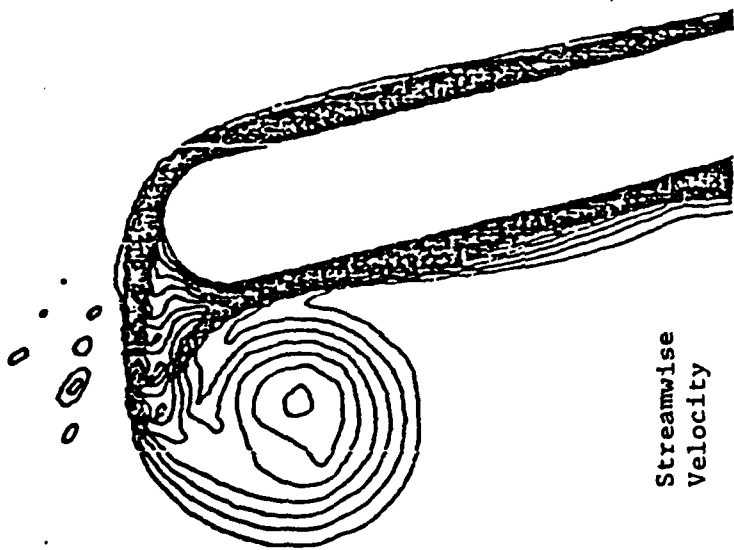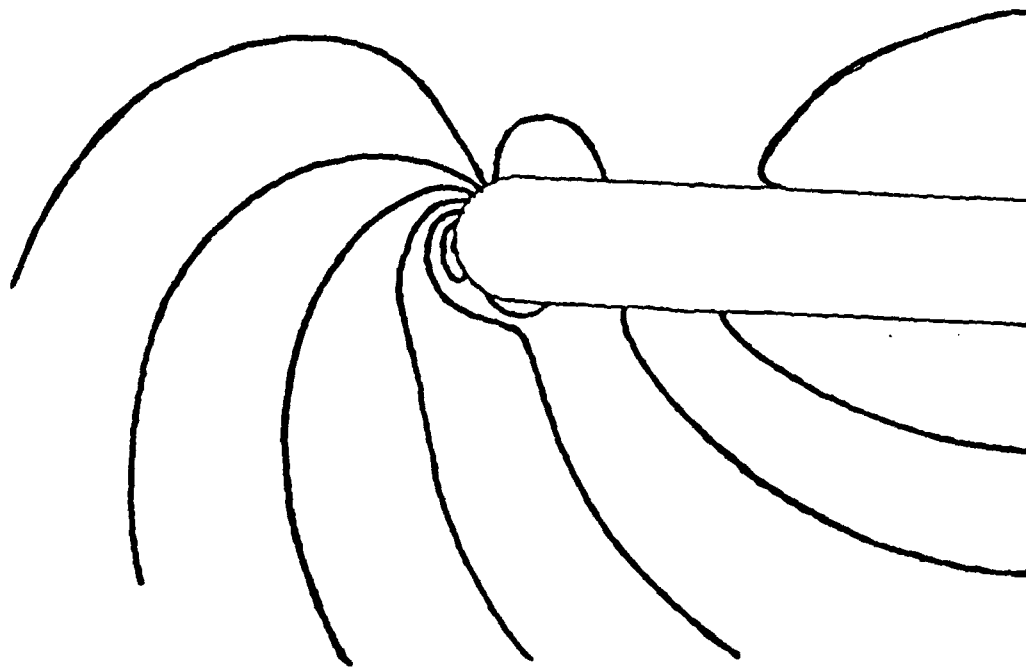
Streamwise
Velocity

Streamwise
Vorticity

Figure 21 - Streamwise station x/t = 20.0

Twisted blade - rotation

42

over the rounded tip onto the suction side. The minimum pressure was computed in the region of the rounded tip. At $x/t = 4.0$, these minimum pressure contours move toward the suction side as the tip vortex begins to form. Figure 23 shows the computed pressure field at two downstream stations, $x/t = 11.0$ and $x/t = 20.0$. At $x/t = 11.0$, the low pressure region has moved to the suction side and a minimum pressure region has formed over the center of the tip vortex. At $x/t = 20.0$, the pressure contours show the further development of the pressure field with the tip vortex. The minimum pressure region continues to be associated with the center of the tip vortex. These computations clearly demonstrate the ability of the PEPSIG code to compute the pressure field associated with the tip vortex and compute the low pressure region at the center of the vortex. This low pressure field would determine the cavitation characteristics of the propeller tip flow field. Figure 24 shows a streamwise contour plot of the computed pressure field on the suction side of the blade. Superimposed on this figure is the track of the vortex obtained from the computations. After an initial transient in the pressure field, the formation of the low pressure region along the vortex track is evident. The resulting track is qualitatively as expected.

Typical computer run times for the tip vortex flow field computations were about 120 seconds for the straight blade cases and about 160 seconds for the twisted blade case. These computations were carried out on a CRAY-1 computer system.
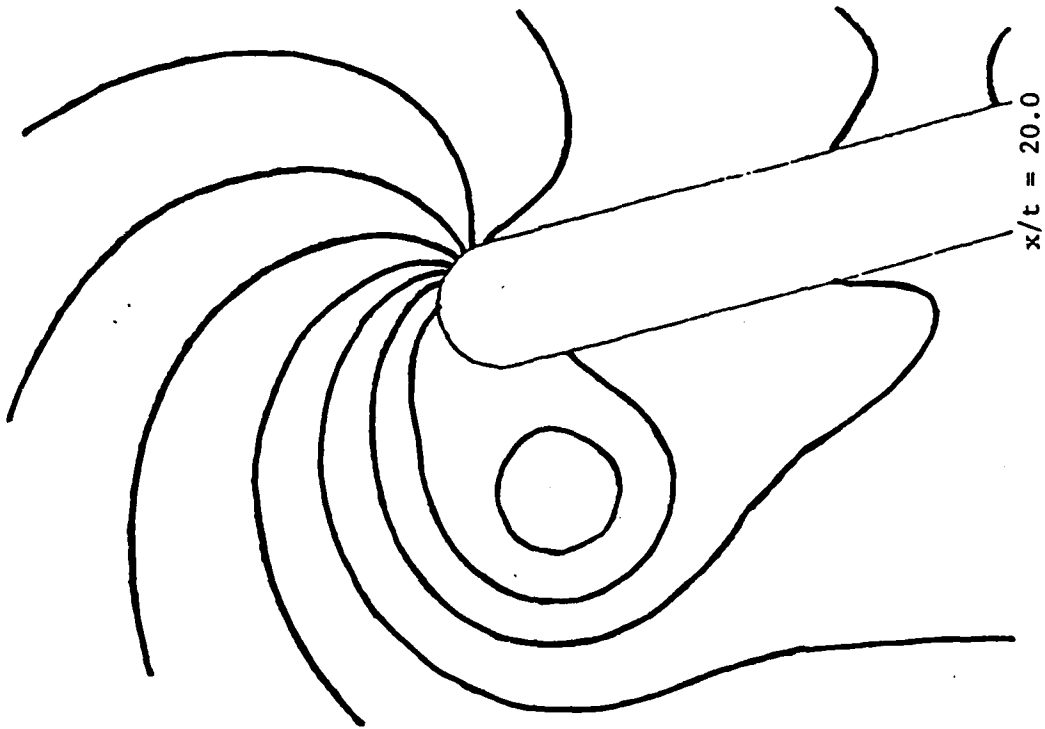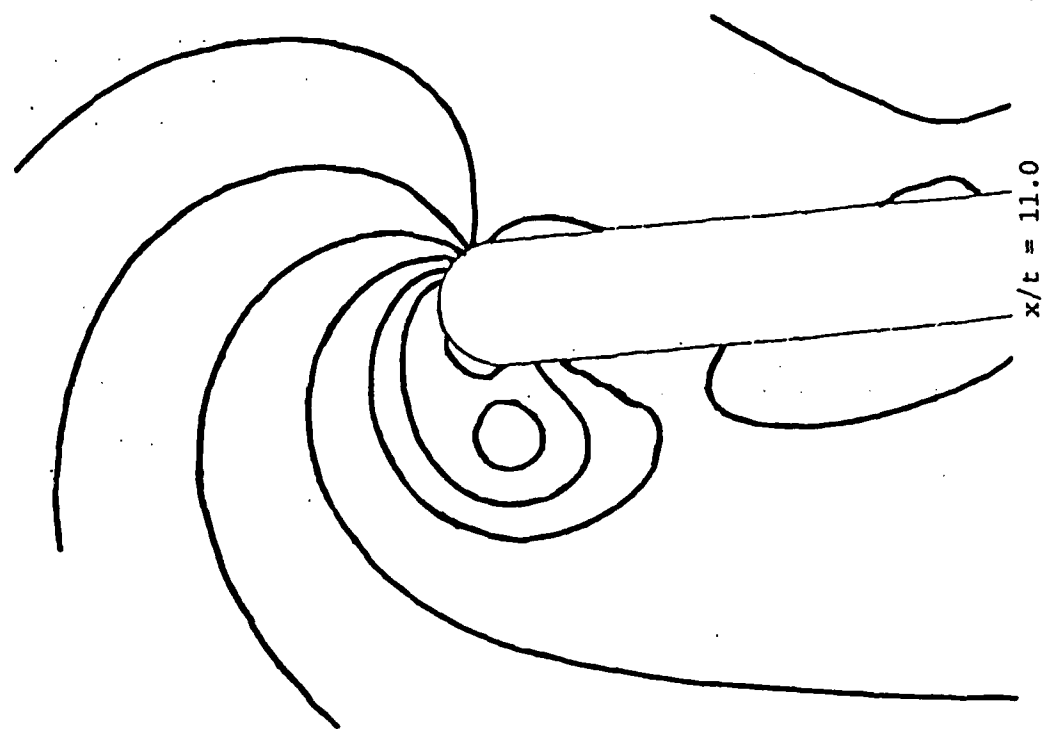
43
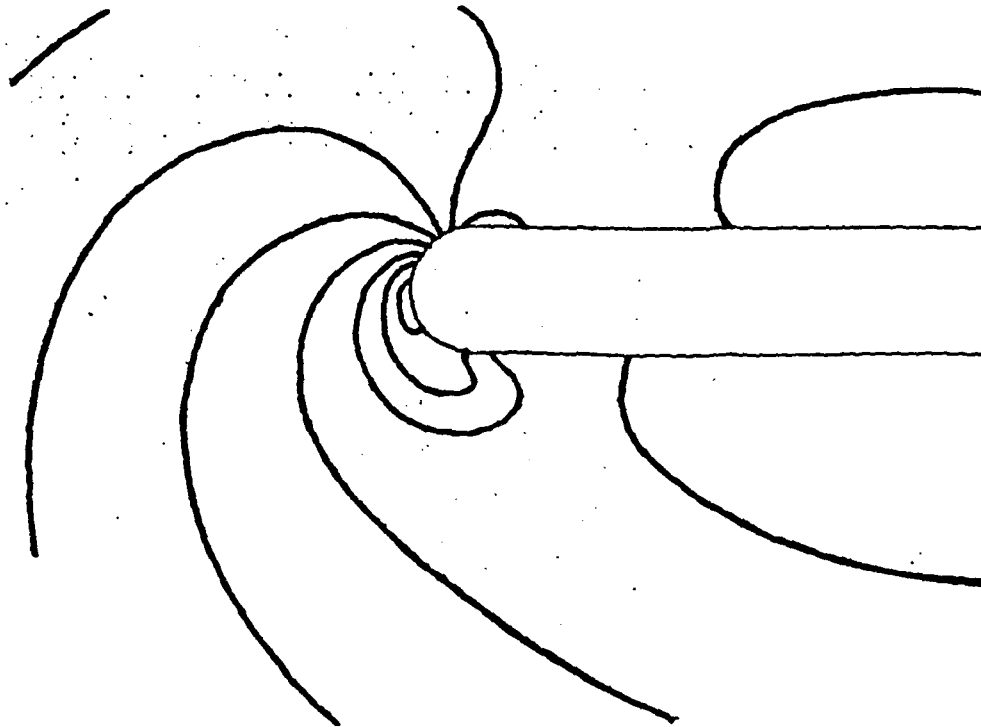
x/t = 4.0

x/t = 2.0

Figure 22 – Transverse Pressure Field

Twisted blade – rotation

44

Figure 23 – Transverse Pressure Field

x/t = 20.0

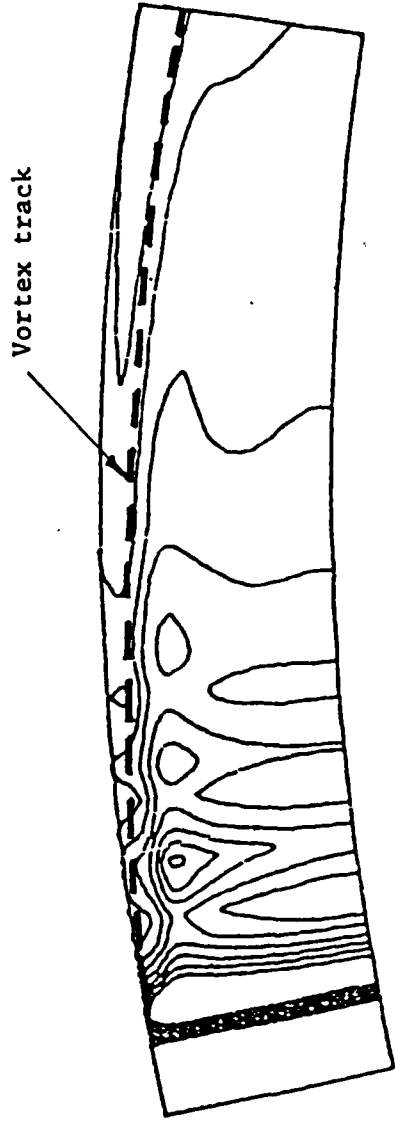x/t = 11.0

Twisted blade – rotation

Vortex track

Flow

Figure 24 - Streamwise contours of the pressure field

(suction side)

46

5. CONCLUSIONS

1. The Phase I effort has demonstrated the feasibility of computing the tip vortex generation process for ship propeller blades by a forward marching procedure.

2. The results also show the capability of the forward marching procedure to compute the low pressure region in the flow associated with the tip vortex. The computation provides the capability of identifying low pressure regions in the flow field that may be susceptible to cavitation.

6. FUTURE EFFORT

The Phase I effort has demonstrated the capability of the forward marching procedure to compute the tip vortex generation process for ship propeller blades. The extension of this capability to providing a computation tool for the scientists and engineers to predict and analyse the tip flow field would be an overall objective of a future effort. Specific tasks that would comprise this effort are the following:

1. Incorporate an inviscid flow analysis to produce a three-dimensional pressure field. The streamwise pressure gradient computed from this pressure field would be input to the viscous flow analysis.

2. Incorporate a mixing length turbulence model suitable for the tip flow field to enable computation of turbulent flow fields.

3. Verify the computations by comparisons with experimenal data.

4. Add geometric capability to the code to handle specific tip shapes, blade thickness distribution, and blade camber.

5. Provide a user-friendly computer code.

The above tasks have been detailed in a Phase II proposal.

REFERENCES

1. Kreskovsky, J.P., Briley, W.R. and McDonald, H.: <u>Prediction of Laminar</u>
    <u>and Turbulent Primary and Secondary Flows in Strongly Curved Ducts</u>,
    NASA CR-3388, February 1981.

2. Levy, R., Briley, W.R. and McDonald, H.: "Viscous Primary/Secondary
    Flow Analysis for Use with Nonorthogonal Coordinate Systems".
    AIAA Paper 83-0556, 1983.

3. Briley, W.R. and McDonald, H.: "On the Structure and Use of Linearized
    Block Implicit Schemes", Journal of Computational Physics, Vol. 34,
    1980.

4. Speziale, C.G.: "Numerical Study of Viscous Flow in Rotating
    Rectangular Ducts", J. Fluid Mech., Vol. 122, pp. 251-271, 1982.

5. McDonald, H., Briley, W.R. and Lin, S.-J.: Initial Value Analysis for
    Rotating Flows in Radial Turbomachinery, Semi-Annual Report, Contract
    No. DAAG29-82-C-0021, Army Research Office.

6. Francis, M.S. and Kennedy, D.A.: "Formation of a Trailing Vortex",
    J. Aircraft, Vol. 16, No. 3, 1979.

7. Chigier, N.A. and Corsiglia, V.R.: "Tip Vortices - Velocity
    Distributions", 27th Annual National V/STOL Forum, American Helicopter
    Society, Washington, DC, 1971.

8. Jessup, S.D.: <u>Measurements of Pressure Distribution on Two Model</u>
    <u>Propellers</u>, DWTNSRDC-82/035.

FILMED